Solar Phys (2008) 247: 123–150
DOI 10.1007/s11207-007-9085-4

A New Model for Propagating Parts of EIT Waves: A Current Shell in a CME

C. Delannée · T. Török · G. Aulanier · J.-F. Hochedez

Received: 4 January 2007 / Accepted: 2 November 2007 / Published online: 28 November 2007

Abstract EIT waves are observed in EUV as bright fronts. Some of these bright fronts propagate across the solar disk. EIT waves are all associated with a flare and a CME and are commonly interpreted as fast-mode magnetosonic waves. Propagating EIT waves could also be the direct signature of the gradual opening of magnetic field lines during a CME. We quantitatively addressed this alternative interpretation. Using two independent 3D MHD codes, we performed nondimensional numerical simulations of a slowly rotating magnetic bipole, which progressively result in the formation of a twisted magnetic flux tube and its fast expansion, as during a CME. We analyse the origins, the development, and the observability in EUV of the narrow electric currents sheets that appear in the simulations. Both codes give similar results, which we confront with two well-known SOHO/EIT observations of propagating EIT waves (7 April and 12 May 1997), by scaling the vertical magnetic field components of the simulated bipole to the line of sight magnetic field observed by SOHO/MDI and the sign of helicity to the orientation of the soft X-ray sigmoids observed by *Yohkoh*/SXT. A large-scale and narrow current shell appears around the twisted flux tube in the dynamic phase of its expansion. This current shell is formed by the return currents of the system, which separate the twisted flux tube from the surrounding fields. It intensifies as the flux tube accelerates and it is co-spatial with weak plasma compression. The current density integrated over the altitude has the shape of an ellipse, which expands and rotates when viewed from above, reproducing the generic properties of propagating EIT waves. The timing, orientation, and location of bright and faint patches observed in the two EIT waves are remarkably well reproduced. We conjecture that propagating EIT waves are the obser-

C. Delannée (✉) · J.-F. Hochedez
Royal Observatory of Belgium, Brussels, Belgium
e-mail: ceaulanier@wanadoo.fr

T. Török
Mullard Space Science Laboratory, University College London, Holmbury St. Mary, Dorking, Surrey, RH5 6NT, UK

G. Aulanier
LESIA, Observatoire de Paris, CNRS, UPMC, Université Paris Diderot, 5 place Jules Janssen, 92190 Meudon, France

vational signature of Joule heating in electric current shells, which separate expanding flux tubes from their surrounding fields during CMEs or plasma compression inside this current shell. We also conjecture that the bright edges of halo CMEs show the plasma compression in these current shells.

Keywords MHD · Sun: corona · Sun: coronal mass ejections (CMEs) · Sun: magnetic fields · Sun: activity · Sun: flare

1. Introduction

EIT waves have been named after the fact that they look like wavelike structures propagating on the solar surface, with a length scale of the solar radius, when observed with the EIT instrument onboard SOHO in 195 Å (Thompson *et al.*, 1998). They originate from flaring active regions. The EIT 195 Å filter contains the Fe XII spectral line emission, formed at coronal temperatures. Therefore, EIT waves are coronal structures. They are associated with two other wavelike structures: Moreton waves and SXR waves. The former are observed in Hα (*i.e.*, in a chromospheric spectral line emission). The latter are observed in soft X rays (*i.e.*, in the hot corona), using the SXT and SXI telescopes onboard the *Yohkoh* and GOES satellites, respectively. Moreton waves velocities were estimated in the range 550 – 2500 km s^{-1} by Moreton (1960) from time and location of both the flare site and the first appearance of the wave front. EIT wave velocities, in contrast, are typically 200 – 400 km s^{-1} (Klassen *et al.*, 2000). Therefore, EIT and Moreton waves seemed to be different structures. However, these three types of wavelike structures show approximately the same behavior: their fronts are bright and arc-shaped, they rarely cover a full circle, and they become fainter and broader during their propagation. Moreover, Thompson *et al.* (2000a, 2000b), Warmuth *et al.* (2004), and Delannée, Hochedez, and Aulanier (2007) showed that wavelike structures associated with solar flares observed in various spectral bands for a same event are co-spatial, indicating that they are "signatures of the same physical disturbance." Finally, Warmuth *et al.* (2004) also showed that the observed structures are not produced exactly at the flare site and are always decelerating. They concluded that this explains the apparent velocity discrepancy between Moreton and EIT waves since the Moreton wave velocities were overestimated and EIT waves are usually observed further away from the flare site than Moreton waves. Zhukov and Auchère (2004) and Balasubramaniam, Pevtsov, and Neidig (2007) showed that all three wave types are coronal structures formed at coronal temperatures. Wills-Davey and Thompson (1999) claim that there is strong evidence of heating of the material in the wave front. Because the wave front is observed in several spectral emission lines, it could also be an enhanced density structure. However, to our knowledge, there exists no observation yet that would clearly show whether a density enhancement or a heating process is responsible for the appearance of wave fronts.

Very few events display a clearly propagating EIT wave with an almost circular shape; only four have been reported so far (Thompson *et al.*, 1998, 1999, 2000a, 2000b). The detailed analysis of one of them, however, revealed patches of weaker and stronger brightness (Podladchikova and Berghmans, 2005); that is, the circle was not fully complete and presented gaps of brightness. These four EIT waves were all related to a flare and a filament eruption. They occurred at the very beginning of the solar cycle (*i.e.*, when the Sun was almost free of other active regions). All other EIT waves observed so far had a quite small angular width and they all appeared when the Sun was very active. Warmuth *et al.* (2004) studied 12 of these EIT waves and found their angular width to be

60° on average. Several authors have recently reported some stationary brightenings in EIT waves, which appear on the way of their propagation and remain at the same location for several minutes (Delannée, 2000; Delannée, Hochedez, and Aulanier, 2007; Attrill *et al.*, 2007; O. Podladchikova, private communication).

Owing to their association with flares, propagating EIT waves are often interpreted as fast-mode magnetosonic waves originating from the flare-related pressure pulse (Uchida, 1968; Wang, 2000; Wu *et al.*, 2001, 2005). These models interpret the stationary patches, which are observed at the edge of distant coronal holes and active regions, as a signature of wave refraction at strong gradients of the Alfvén speed (Wang, 2000; Ofman and Thompson, 2002). Even though the magnetosonic wave model is often used, it is not supported by observations. First, these models were never successfully applied to noncircular EIT waves. Second, Delannée and Aulanier (1999), Cliver *et al.* (2005), and Chen (2006) showed that very few flares, even among the most intense ones, are associated with EIT waves. Third, many stationary brightenings are not located at the edge of coronal holes nor in active regions; rather they are found in the quiet Sun, where the spatial variation of the Alfvén velocity is expected to be very smooth. It has been shown that stationary brightenings of EIT waves are indeed located at the footpoints of jumps of magnetic field line connectivity (Delannée and Aulanier, 1999; Delannée, Hochedez, and Aulanier, 2007). Fourth, by taking into account the data gaps and uncertainties owing to poor observations, Delannée and Aulanier (1999) and Biesecker *et al.* (2002) showed that 100% of EIT waves are associated with a coronal mass ejection (CME). Even though the last finding led Warmuth (2007) to consider that EIT waves could still be magnetosonic waves, triggered by the abrupt and fast launch of a CME instead of a flare pressure pulse, the problem of the stationary parts, which is often omitted in EIT wave studies, persists in this interpretation.

These inconsistencies of the magnetosonic wave interpretation led Delannée and Aulanier (1999) and Chen *et al.* (2002) to propose that propagating EIT waves could be the signature of the gradual opening of magnetic field lines during CMEs and that their stationary parts could be associated with the large-scale structure of the pre-eruptive magnetic field.

The latter point was analyzed in detail in Delannée and Aulanier (1999) and Delannée, Hochedez, and Aulanier (2007) for two different EIT waves. Using potential magnetic field extrapolation, they showed that the stationary parts of these EIT waves are cospatial with areas of drastic jumps in the connectivities of the magnetic field called separatrices or quasi-separatrices, depending on how discontinuous or drastic the jumps are. The EUV brightenings were related to Joule heating occurring in narrow electric current sheets that are known to develop very easily in (quasi-) separatrices when any perturbation (such as a CME) disturbs the potential fields (see Low and Wolfson, 1988; Démoulin, 2006; Aulanier, Démoulin, and Grappin, 2005; Aulanier, Pariat, and Démoulin, 2005). We note that whether such current sheets indeed play a role in increasing the coronal emission is still an unanswered question. Nevertheless, the collocation of electric currents and of coronal brightenings has been put forward in sigmoid models (Magara and Longcope, 2001; Aulanier, Démoulin, and Grappin, 2005; Aulanier, Pariat, and Démoulin, 2005) and a simulated temperature map resulting from Joule heating during reconnection was successfully compared to cusp structures observed in soft X rays during CMEs (Shiota *et al.*, 2005). From these studies, one could conjecture that Joule heating may indeed play a role in the corona, at least at small scales as in current sheets in which electric currents can be very high and the magnetic Reynolds number can be very low, a typical property of weakly resistive plasmas. As was done for stationary EIT waves, the nature of propagating circular bright fronts of EIT waves also needs to be understood, and tested against observations, in terms of magnetic field motions that can produce narrow electric currents.

To do so, we perform two three-dimensional (3D) MHD simulations of a bipolar coronal magnetic flux tube that is twisted by slow photospheric vortex motions centered at the two photospheric flux concentrations of the bipole, using two independent numerical codes. This model is known to result, after a quasi-static phase, in a very fast upward expansion of current-carrying magnetic fields in the corona, at a rate that is much larger than the prescribed twisting motions (Amari *et al.*, 1996; Török and Kliem, 2003; Aulanier, Démoulin, and Grappin, 2005; Aulanier, Pariat, and Démoulin, 2005). The applicability of the model for solar eruptions has some limitations (for detailed discussion, see Török and Kliem, 2003; Aulanier, Démoulin, and Grappin, 2005; Aulanier, Pariat, and Démoulin, 2005). First, the flux tube expansion is continuously driven by photospheric vortex motions, which are not observed very frequently (see, *e.g.*, Brown *et al.*, 2003). Second, no release of magnetic energy, as required in flares, takes place in these models. However, it is useful to investigate the magnetic field expansion in the model for our purpose for the following reasons. First, the model nicely reproduces the exponential-to-linear rise characteristic often observed in CMEs (*e.g.*, Vršnak, 2001). Second, since no reconnecting current sheet readily forms in the wake of the expanding flux tube, it does not lead to an eruptive flare, and so everything that happens in the dynamic phase is solely due to the fast magnetic field line expansion. As will be shown in the following, this suggests that EIT waves may not be related to flares but may be related to CMEs alone. Third, the simplicity of the model, its 3D nature, and the robustness of the results tested with both codes permit the derivation of generic properties that can be tested against any observation of a CME launched from an isolated active region, as is the case for all well-known propagating quasi-circular EIT waves.

This paper is organized as follows. In Section 2 we describe the numerical setups for both MHD simulations. In Section 3 we describe the dynamics of the twisted flux tube and we analyze the formation of current layers during the simulation. We show that a large-scale, narrow, and intense current shell forms at the beginning of the dynamic phase, within the initially extended and weak return currents that naturally separate the twisted flux tube from the surrounding potential fields. We also show that the current shell is co-spatial with an enhanced-density shell generated by plasma compression. In Section 4 we analyze the observational properties of this current shell viewed from above (*i.e.*, in projection on the solar disk). In Section 5 we discuss how this simple and generic model captures the essential features of propagating EIT waves. We argue that, in spite of all our disputable assumptions, the modeled current shell remarkably fits the observed EIT waves well. In Section 6, we discuss the plausible association between the bright edges of halo CMEs with the enhanced-density shell. We present our conclusions in Section 7.

2. Setup for the MHD Simulations

2.1. Overview of the Codes

We use two independent 3D MHD codes, extensively described in Török and Kliem (2003), Aulanier, Pariat, and Démoulin (2005) and in Aulanier, Démoulin, and Grappin (2005). In the following, we refer to these codes as TK and ADG, respectively, and we qualitatively recall their main features. For more details, we refer the reader to the related papers.

Both codes calculate the nondimensionalized zero-β MHD equations in Cartesian geometry:

$$\frac{\partial \rho}{\partial t} = \nabla \cdot (\rho \mathbf{u}) + \mathcal{D}^{\rho}, \tag{1}$$

$$\rho \frac{\partial \mathbf{u}}{\partial t} = \rho(\mathbf{u} \cdot \nabla)\mathbf{u} + \mathbf{J} \times \mathbf{B} + \mathcal{D}^{\mathbf{u}}, \tag{2}$$

$$\frac{\partial \mathbf{B}}{\partial t} = \nabla \times (\mathbf{u} \times \mathbf{B}) + \mathcal{D}^{\mathbf{B}}, \tag{3}$$

$$\mathbf{J} = \nabla \times \mathbf{B}, \tag{4}$$

where ρ and $\mathbf{J}$ are the mass and electric current densities, respectively, $\mathbf{u}$ and $\mathbf{B}$ are the velocity and magnetic fields, respectively, and $\mathcal{D}^A$ are diffusive operators. (For a description of the normalization we refer to the TK and ADG papers).

In TK, the equations are written in conservative form, whereas in ADG they are fully developed by removing all $\nabla \cdot \mathbf{B}$ terms. Both codes are fully explicit; TK uses a modified low-order two-step Lax – Wendroff scheme whereas ADG uses a high-order finite difference predictor – corrector scheme to solve the equations. Both codes use nonuniform grids.

Both codes incorporate a diffusive operator $\mathcal{D}^{\mathbf{u}}$ for the velocity components u_i, which redistributes to every mesh point a small fraction of u_i from the neighboring points at each time step. Neither code smooths the mass density [although note that in Török and Kliem (2003) smoothing of $\rho\mathbf{u}$ and ρ was used, which was required by the very long lasting relaxation runs performed in that work]. ADG uses a Laplacian term for the magnetic diffusion $\mathcal{D}^{\mathbf{B}}$, with a constant and weak resistivity η. TK does not smooth the magnetic field, but it does incorporate viscosity. Still, some numerical magnetic diffusion occurs in TK because of its low-order scheme.

Both codes use line-tied boundary conditions at $z = z^\circ$, but they use them differently. TK describes the boundary conditions in the ghost cells $(x, y, -\Delta z)$ and applies some extra smoothing in the first mesh points above $z = z^\circ$. ADG fixes its boundary right at $z^\circ = 0$ and uses conditions on the normal derivatives of all quantities to ensure line-tying conditions.

The TK scheme allows the use of highly stretched nonuniform grids; therefore the domain of computation is very large in this code. Closed boundary conditions are imposed at the lateral boundaries (*i.e.*, there are no plasma flows through these boundaries). We use a smaller domain with ADG, but with a higher spatial resolution. The ADG scheme does not imply a confinement from the outer boundaries since it allows outflows and inflows.

Even though the two coded incorporate the same physics, they are clearly different. Using both TK and ADG is motivated by checking upon the reliability of the results, since the most important features that we study occur in a highly nonlinear dynamic phase in which the velocities are of the order of the Alfvén speed. Indeed, sharp velocity and magnetic field gradients develop during the dynamic phase and these may lead to different numerical behavior depending on the code (as discussed in Aulanier, Démoulin, and Grappin, 2005; Aulanier, Pariat, and Démoulin, 2005).

2.2. Initial Magnetic Field and Boundary Driving

We use a Cartesian domain (x, y, z) where the z axis is the altitude in the solar corona and the $z = 0$ plane is supposed to be the solar photosphere. With the TK code, we use $x \in [-100, 100]$, $y \in [-100, 100]$, and $z \in [0, 200]$ and the mesh has $n_x \times n_y \times n_z = 195 \times 329 \times 150$ grid points including the ghost cells. With the ADG code, we use $x \in [-15, 15]$, $y \in [-15, 15]$, and $z \in [0, 30]$ and the mesh has $n_x \times n_y \times n_z = 231 \times 231 \times 231$ grid points. Both meshes are nonuniform with the largest concentration of grid points being located at low altitudes and in the center of the box.

The initial potential field $\mathbf{B}^\circ$ and the initial mass density ρ° analytically result from the sum of two subphotospheric monopoles $\mathbf{B}^+$ and $\mathbf{B}^-$, located at $(0, \pm 1, -1)$, having equal

magnetic flux F and opposite signs. Their expressions are

$$\mathbf{B}^{\circ} = \mathbf{B}^{+} + \mathbf{B}^{-}, \tag{5}$$

$$\mathbf{B}^{\pm} = \pm F\mathbf{r}^{\pm}/|\mathbf{r}^{\pm}|^{3}, \tag{6}$$

$$\mathbf{r}^{\pm} = (x, y \mp 1, z + 1), \tag{7}$$

$$\rho^{\circ} = |\mathbf{B}^{\circ}|^{2}, \tag{8}$$

where F is chosen so as to result in $\max[B^{\circ}] = 1$. With these settings, the photospheric bipolar magnetic field has its positive (negative) polarity centered at $x = 0$ and $y \approx +1$ (-1), respectively. We choose the distance between the monopoles, $L = 2$, as the characteristic length of the system. The initial Alfvén speed is $c_{\mathrm{A}}^{\circ} = 1$ everywhere in the box. This permits us to define a characteristic Alfvén time of $t_{\mathrm{A}} = L/c_{\mathrm{A}}^{\circ} = 2$. The magnetic field strength decreases like z^{-3} at high altitudes.

The system is driven at the line-tied plane with a slow and incompressible two-dimensional photospheric velocity field $\mathbf{u}_{\perp}$. This velocity is directly prescribed in the plane $z = z^{\circ}$ and it is given by

$$\mathbf{u}_{\perp}(x, y, t) = \psi^{\circ} f^{i}(t) \nabla\psi(x, y) \times \mathbf{e}_{z}, \tag{9}$$

$$\psi(x, y) = B_{z}^{\circ 2}\big(z = z^{\circ}\big) \times \exp\left[\frac{B_{z}^{\circ 2}(z = z^{\circ}) - [B_{z}^{\circ 2}(z = z^{\circ})]_{\max}}{9[B_{z}^{\circ 2}(z = z^{\circ})]_{\max}}\right], \tag{10}$$

where t is the time, $\mathbf{e}_{z}$ is the unit vector along the z axis, and ψ° is a free parameter, which we chose to set $\max[u_{\perp}] = u^{\circ} = 0.02\, c_{\mathrm{A}}^{\circ}$. By definition, this driving ensures that $\partial B_{z}^{\circ}(z = z^{\circ})/\partial t = 0$, so that the photospheric distribution of flux is preserved throughout the calculations. The function $f^{i}(t)$ is a ramp function that allows the driving velocities to progressively reach their stationary values at early times, so as to avoid the launch of steep shocks from the line-tied boundary. ADG uses a smooth ramp,

$$f^{\mathrm{ADG}}(t) = \frac{1}{2}\tanh\left[\frac{2}{5}(t - 15)\right] + \frac{1}{2}, \tag{11}$$

which allows the system to relax to a numerical equilibrium for $t < 10$ and to be driven at a constant speed for $t > 20$. TK uses a simpler linear ramp,

$$f^{\mathrm{TK}}(t) = \frac{t}{20} \quad \text{for } t \le 20, \tag{12}$$

$$f^{\mathrm{TK}}(t) = 1 \quad \text{for } t > 20, \tag{13}$$

which also leads to a constant driving speed for $t > 20$.

3. Dynamics, Electric Currents, and Plasma Compression

As described in Section 1, the observed wavelike structures are coronal and chromospheric brightenings. Two factors can lead to multiwavelength brightenings: a density increase or a temperature increase. The density increase may result from compressive motions whereas

the heat may a priori result from adiabatic effects (owing to compression) or from Joule dissipation in strong electric currents. Therefore, we concentrate our study on the possible appearance of electric currents and plasma compression caused by the expansion of a twisted magnetic flux tube. The flux tube expansion is described in Section 3.1, the electric currents in Section 3.2, and the plasma compression in Section 3.3. We always compare the results of both simulations to test for similarities and differences between them.

3.1. Expansion of the System

As twist is continuously injected into the system, it evolves within three regimes (see Figure 1). For $0 \leq t \leq 46$ the evolution is quasi-static. The twisted flux tube is formed and its expansion starts, but very slowly. For $46 \leq t < 96$, the evolution is highly dynamic: the expansion of the flux tube becomes very fast. Figure 1 (left plot) shows that at $t \approx 96$, the rise velocity of the flux tube (measured at the apex of its axis) starts to saturate. A complementary simulation done with TK, using an additional weak density smoothing to ensure numerical stability, showed that the velocity becomes constant at $\approx 1.15\, c_{\mathrm{A}}$ after $t = 96$. We expect that a slightly higher constant speed would be reached in TK and ADG if the TK simulation would not become unstable before and if a larger box of computation were used in ADG. In ADG, the apex of the flux tube passes through the upper boundary at $t = 106$. In TK, the simulation becomes unstable at $t = 106$, when the altitude of the flux tube axis apex is $z = 36$. Note that the flux tube has a slightly different dynamic in the two simulations: in TK it reaches slightly greater heights for the same times than in ADG. This is most likely due to the somewhat different driving ramp applied to the system.

Figures 2 and 3 show 3D frames resulting from the simulations of ADG and TK, respectively. As the resistivity is zero at $z = z^{\circ}$, the magnetic field lines cannot reconnect at this

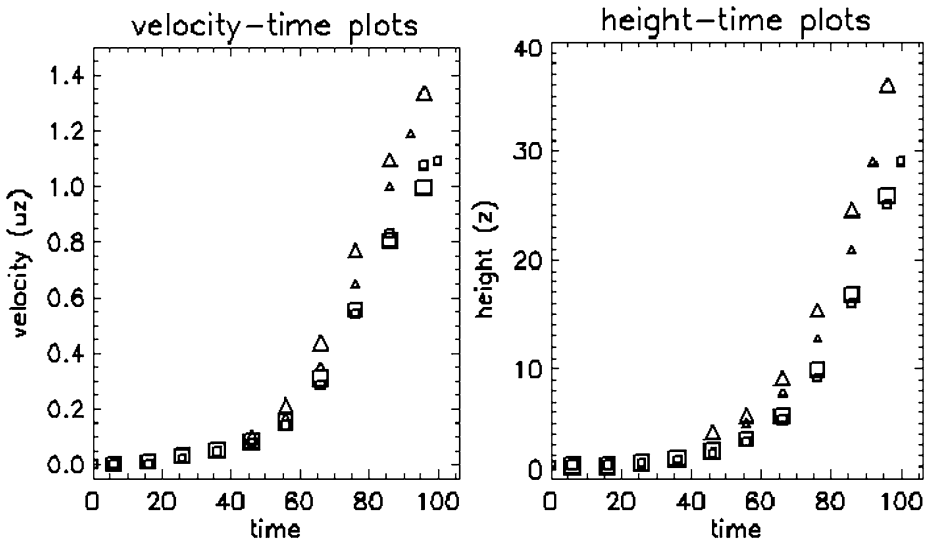

Figure 1 Rising velocity (left) and altitude (right) of the center of the twisted flux tube (squares) and the top of the current shell (triangles) in TK (large features) and in ADG (small features). The results of both simulations are similar. The twisted flux tube is expanding in height, with its velocity increasing until it shows a tendency toward saturation at $u_z \approx 1.15\, c_{\mathrm{A}}$. The current shell is expanding in front of the flux tube. The distance between the flux tube center and the current shell is increasing with time.

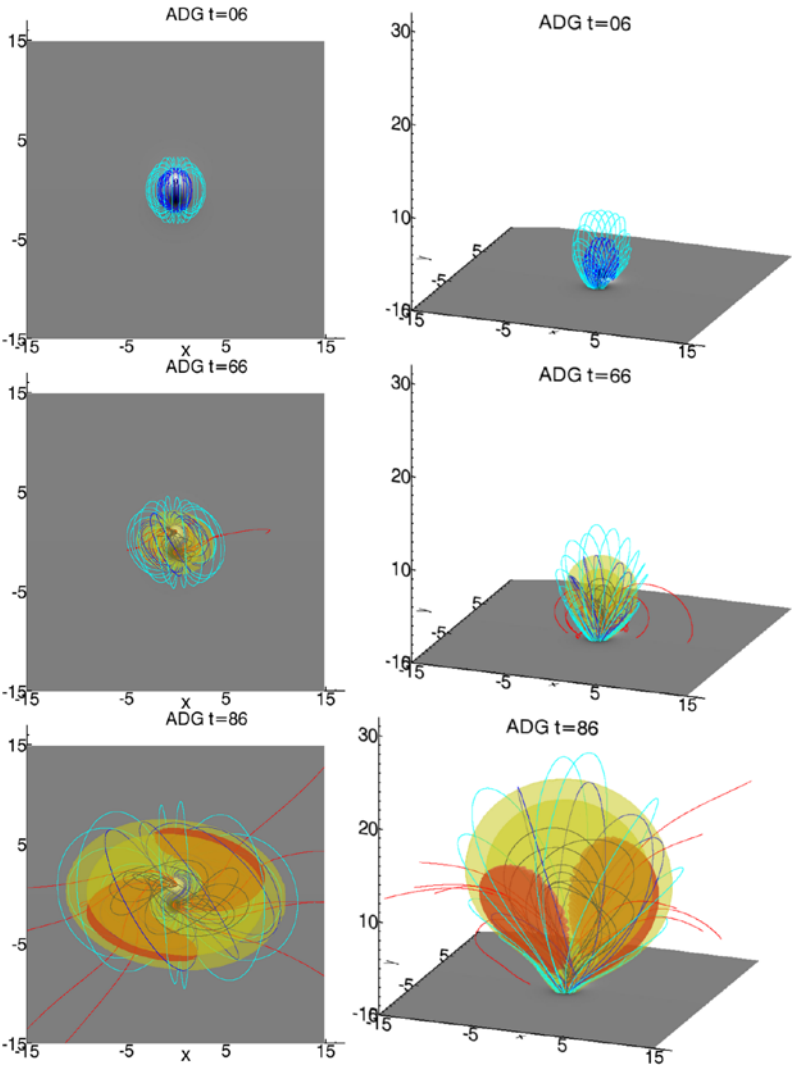

Figure 2 Numerically relaxed bipolar potential field at $t = [6]$ and expanding flux tube at $t = [66; 86]$ for ADG. The full numerical domain is shown, as viewed from above (along the z axis; left) and in projection (right). The plotted magnetic field lines are rooted in $B_z(z = 0) = 0.3$ (cyan lines), 0.5 (blue lines), and 0.9 (dark blue lines). Selected velocity streamlines are plotted in red. Transparent isosurfaces of $\mathbf{J} \cdot \mathbf{B}/B^2 = 0.5$ (1.9 and -1.9) are drawn in yellow (red and green), respectively. These surfaces show the formation of the current shell surrounding the expanding flux tube.

altitude, so they are following the twisting motions. The latter are transmitted above $z = 0$, progressively twisting the magnetic flux tube. Its most twisted part (located near its central axis) is shown in Figures 2 and 3 as the dark-blue magnetic field lines that are rooted in the isocontour $B_z(z = 0) = 0.9$. Blue magnetic field lines rooted in $B_z(z = 0) = 0.5$ show the outer part of the twisted flux tube. Cyan field lines rooted in $B_z(z = 0) = 0.3$ remain almost untwisted, and hence potential, during the whole simulation.

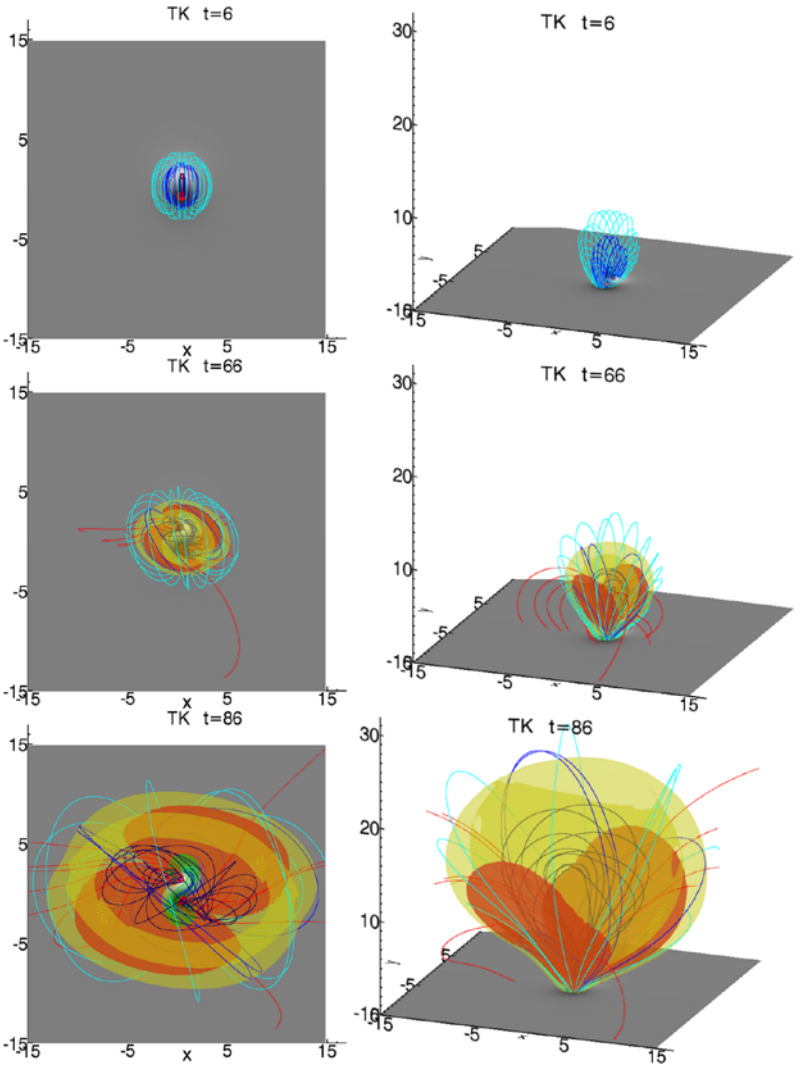

Figure 3 Same as Figure 2 for TK. The color-coding and parameter values are identical to Figure 2 except for the red transparent isosurfaces, which correspond to $\mathbf{J} \cdot \mathbf{B}/B^2 = 1.2$ here. The evolution of the twisted flux tube and the formation of the narrow return electric currents in the outer layer of the flux tube are similar to those of ADG.

As shown by velocity streamlines (drawn in red in the images at $t = [66, 86]$ in Figures 2 and 3), the twisted magnetic flux tube expands upwards and sidewards. The upward motion can be explained as follows. At $t = 0$, the magnetic field is potential. Aly (1989) demonstrated that the potential magnetic field corresponds to a minimum of the magnetic energy. Since in both simulations $B_z(z = z^\circ)$ remains unchanged and the magnetic field at the lateral boundaries changes only slightly, the total magnetic energy increases with time. The twist is prescribed only locally; therefore, the magnetic energy density and hence the magnetic pressure both increase mainly in the twisted field lines. This pressure cannot lead to significant downward motion across the lower boundary because the boundary acts like

a wall, so it mostly produces an upward motion of the twisted fields. The potential fields rooted far from the boundary vortices are also moving upwards, since they are pushed from below as the lower lying twisted fields expand.

The increasing magnetic pressure in the low-lying twisted magnetic field lines also leads to horizontal motions and to some downward motions at large distance from the bipole. These motions can be decomposed as follows (see Figures 2 and 3). First, the red velocity streamlines inside the flux tube show the twisting motion above the flux concentrations. Second, the main axis of the flux tube is rotating around the z axis (as explained in Aulanier, Démoulin, and Grappin, 2005; Aulanier, Pariat, and Démoulin, 2005). This is visible by the tendency of the velocity streamlines to spread apart near the apex of the flux tube and to form a second but larger twist pattern between the twisted flux tube core and its outer part. Third, the nearly horizontal streamlines far from the magnetic flux tube reveal the sideward motion of the whole system at moderate altitudes (since the flux tube bulges out in every direction). Some low-lying magnetic field lines are pushed downwards as the twisted flux tube passes above them. Those downward motions are indicated by the streamlines that connect the magnetic bipole boundary and an outer point at $z = 0$.

At large altitudes, the streamlines become almost horizontal as they pass from the twisted to the untwisted regions. So, the untwisted magnetic field lines are not going upwards as fast as the twisted magnetic flux tube core. This can be explained by the fact that the twisting motion injected in the polarities of the magnetic bipole is decreasing with the distance from the center of the polarities. Therefore, the injected magnetic pressure also decreases in the same manner. The difference of velocity between the untwisted and the twisted magnetic field lines leads to an accumulation of magnetic field lines with different twist in the outer part of the twisted flux tube.

3.2. A Narrow Current Shell in the Return Currents

Electric currents develop in the layer of accumulation of magnetic field lines described above and below the twisted flux tube. However, the variations of the current densities at higher altitudes are not contrasted enough to allow a good presentation of their appearance. Moreover, their intensity depends on the intensity of the magnetic field. In contrast, the quantity $\mathbf{J} \cdot \mathbf{B}/B^2$ has a small dependence on the magnetic field intensity and is much more contrasted. In addition, as shown in Figure 4, the current densities are co-spatial with the quantity $\mathbf{J} \cdot \mathbf{B}/B^2$. Therefore, in the following, we analyze $\mathbf{J} \cdot \mathbf{B}/B^2$, which not only shows the electric currents themselves, but which also measures their orientation with respect to the magnetic field and their thickness. ($\mathbf{J} \cdot \mathbf{B}/B^2$ has the dimension of the inverse of a length scale of magnetic field gradients; it is therefore typical of the current sheet thickness.) The higher $\mathbf{J} \cdot \mathbf{B}/B^2$ is, the thinner the currents sheets are and the more efficient the resistive effect are. However, even if the simulation produce high values of $\mathbf{J} \cdot \mathbf{B}/B^2$, the numerical mesh of the simulation does not allow these sheets to get very thin nor allow electric currents to become very strong in these weak field regions. Physically, by analogy with the solar flares, electric currents are expected to be much thinner and stronger in the corona than in the simulation.

The distribution of $\mathbf{J} \cdot \mathbf{B}/B^2$ is shown in Figures 2 and 3 as yellow, red, and green semi-transparent isosurfaces. At $t = 6$, only weak and extended currents are formed ($-0.5 < \mathbf{J} \cdot \mathbf{B}/B^2 < 0$). They are located around the footpoints of the twisted flux tube. Until $t \approx 46$, electric currents are mainly formed in the core of the twisted flux tube (see green isosurfaces of $\mathbf{J} \cdot \mathbf{B}/B^2 = -1.9$ in Figures 2 and 3). These so-called direct currents are flowing antiparallel to the magnetic field (*i.e.*, $\mathbf{J} \cdot \mathbf{B} < 0$). Later, during the flux tube fast expansion,

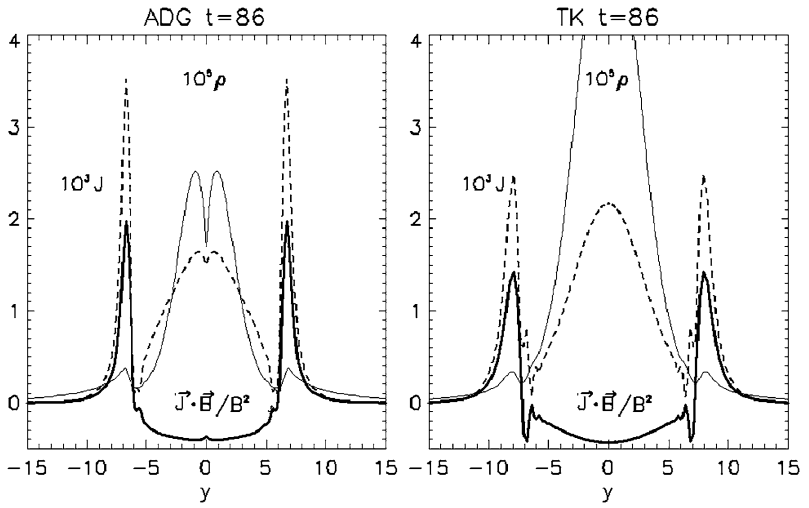

Figure 4 Plots of $10^6 \times \rho$ (thin solid lines), $10^3 \times |\mathbf{J}|$ (dotted lines), and $\mathbf{J} \cdot \mathbf{B}/\mathbf{B}^2$ (thick solid line) with ADG (left) and TK (right) at $t = 86$, $x = 0$, $z = 12$. The peaks of the three quantities, visible at $y \approx \pm 7$ in ADG and $y \approx \pm 8$ in TK, are co-spatial and represent the current and enhanced-density shells in the outer layer of the flux tube.

these direct current densities decrease as the twist per unit length decreases. Meanwhile, other direct currents located below the twisted flux tube slowly increase. They form an extended S-shaped current layer. Aulanier, Démoulin, and Grappin (2005), Aulanier, Pariat, and Démoulin (2005) and Magara and Longcope (2001) related these features to observed soft X-ray sigmoids, which are known to precede some CMEs (Manoharan *et al.*, 1996; Canfield, Hudson, and McKenzie, 1999).

After $t \approx 46$, a narrow current shell develops (see the yellow and red transparent surfaces in Figures 2 and 3). It is formed by return currents (*i.e.*, $\mathbf{J} \cdot \mathbf{B}/B^2 > 0$). Its magnitude significantly increases with time. The return currents at $t = 46$, which already exist at earlier times, are then very broad and weak ($0 < \mathbf{J} \cdot \mathbf{B}/B^2 < 0.5$), but, after $t \approx 76$, $|\mathbf{J} \cdot \mathbf{B}/B^2|$ in the current shell exceeds the values in the twisted flux tube and becomes comparable to the values in the S-shaped current layer. The electric current density and the thickness of the current layer are in the shell of the same order as in the S-shaped current layer. The return currents are located in the outer layer of the twisted magnetic flux tube (*i.e.*, where magnetic field lines of different twists accumulate). Once the current shell is well developed, it expands at large speeds, ahead of the twisted flux tube, not only along the vertical z direction (see Figure 1) but also horizontally (see Figures 2 and 3), following the motion of the magnetic field lines.

The generation of return currents around direct currents, right from the beginning of the twisting motions, is natural in MHD when vortices have a finite extent. The return currents are due to the inversion in sign of the crossing (*i.e.*, shear) angle between adjacent twisted magnetic field lines between the inner to the outer part of the vortex (see, *e.g.,* Mikic, Schnack, and van Hoven (1990) for cylindrical models). Therefore they are located between the edge of the twisted flux tube and the outer magnetic field lines, which remain almost potential during the simulation.

Both the ADG and TK simulations form current shells of similar shapes, but with slight differences. In ADG, the current shell has a smaller thickness than in TK. At $\mathbf{J} \cdot \mathbf{B}/B^2 = 0.5$, the current shell is not closed in TK, whereas it is closed above the flux tube in ADG (see

the yellow semitransparent isosurfaces of $\mathbf{J} \cdot \mathbf{B}/B^2 = 0.5$ at $t = 86$ in Figures 2 and 3). In TK the current shell is closed only for $\mathbf{J} \cdot \mathbf{B}/B^2 \leq 0.45$. As is the case for the twisted flux tube, the current shell expands somewhat faster in TK than in ADG (see Figure 1). In ADG, the current shell crosses the upper boundary ($z = 30$) at $t = 94$, whereas in TK, it reaches an altitude of $z = 36$ at $t = 96$. Apart from these minor quantitative differences, both calculations qualitatively show the same features. In particular, the narrowest current layers within the shell distribute along two 3D lobes (shown as red surfaces in Figures 2 and 3). These lobes are extended in altitude since each of them links the neighborhood of one twisting footpoint at $z = 0$ up to the side of the twisted flux tube at the altitude of its main axis. Therefore, the amplification of the return electric currents in the shell results not only from the global upward and sideward expansion of the twisted flux tube but also from its global rotation with respect to the orientation of the magnetic bipole at $z = 0$.

3.3. Co-Spatial Enhanced-Density Shell

As already described, the twisted flux tube inflates in response to the imposed vortex motions. The overlying field lines that remain almost potential are pushed upwards and sideways by the expanding twisted flux tube. Hence, the velocities of the overlying magnetic field remain much smaller than the velocities inside the twisted flux tube. The velocity streamlines, drawn in red in Figures 2 and 3, are deflected from the vertical to the horizontal direction when they pass through the current shell, showing that there exists a strong variation of the vertical component of the velocities, yielding a compression of the plasma.

Figure 5 shows cuts of the logarithm of the density. Visible is an enhanced-density shell that is co-spatial with the current shell but is obviously less contrasted with its surrounding

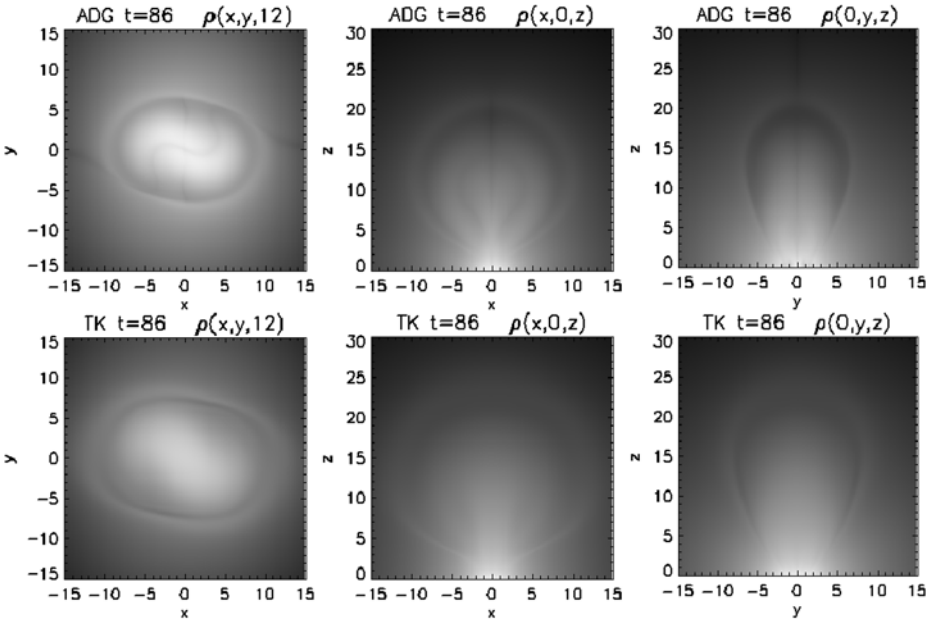

Figure 5 Cuts of $\log(\rho)$ in the planes $(x, y, 12)$, $(x, 0, z)$, and $(0, y, z)$ (from left to right) at $t = 86$ with ADG (top) and TK (bottom). A shell of enhanced density is formed in the outer layer of the twisted flux tube in both simulations.

(see Figure 4). The initial density profile that was set in the calculation to ensure a constant Alfvén speed at $t = 0$ yields a very fast decrease of the density with height. One can expect the enhanced densities within the current shell to remain present if different initial density profiles are used, since they are formed by velocity fields that result from magnetic forces only.

4. Rendering On-Disk Observations

4.1. Integration over the Altitude of the Current Shell

Just as the S-shaped direct currents could result in Joule heating and may be observable as soft X-ray sigmoids, the large-scale narrow shell of return currents could also lead to Joule heating, hence contributing to an enhanced brightness observed in hot emission lines. The enhanced-density shell may also brighten the coronal plasma, since most EUV and soft X-ray filters are responsive to both temperature and density.

The coronal plasma is optically thin in many spectral lines. Therefore, the observation of a structure on the Sun is due to the integration along the line of sight of the brightness of the plasma. Neither optical nor thermodynamical values can be derived from the results of the studied simulations; therefore we integrate $\mathbf{J} \cdot \mathbf{B}/B^2$ along the altitude z to render what would be observed if the narrow shell of return currents would be dissipated via Joule heating. The resulting integrations, $\int \mathbf{J} \cdot \mathbf{B}/B^2 \, \mathrm{d}z$, are plotted in Figures 6 and 7. In these figures, both white and black stand for strong emissions, with $\int \mathbf{J} \cdot \mathbf{B}/B^2 \, \mathrm{d}z > 0$ and < 0, respectively. Weak coronal emissions (*i.e.*, $\int \mathbf{J} \cdot \mathbf{B}/B^2 \, \mathrm{d}z \approx 0$) are shown in gray.

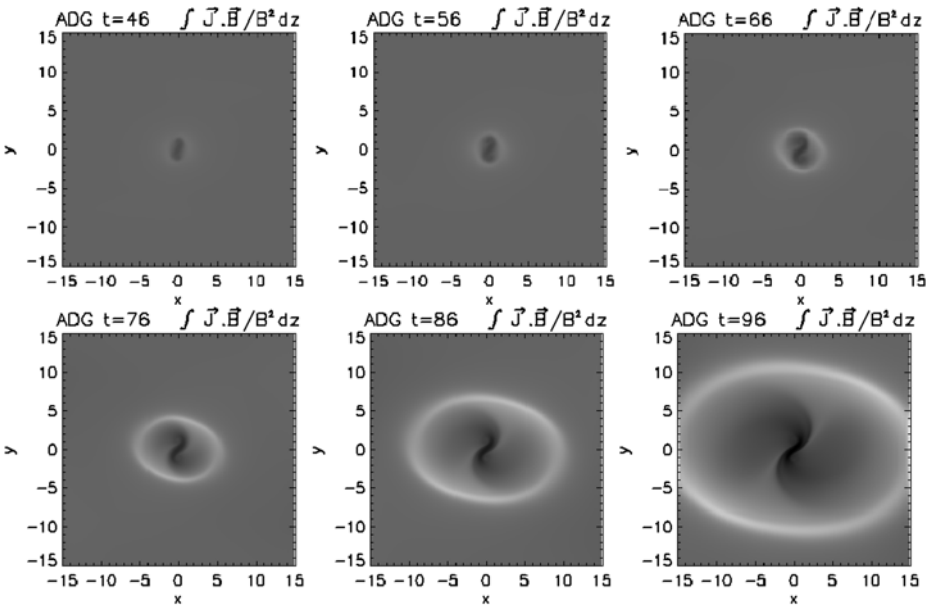

Figure 6 Frames of $\int \mathbf{J} \cdot \mathbf{B}/B^2 \, \mathrm{d}z$ at $t = [46; 56; 66; 76; 86; 96]$ for ADG. The linear scaling of the intensity is the same in all frames. Positive values are shown in white and negative values are shown in black. The integration along the altitude of the current shell reveals an ellipse, which is expanding and rotating with time.

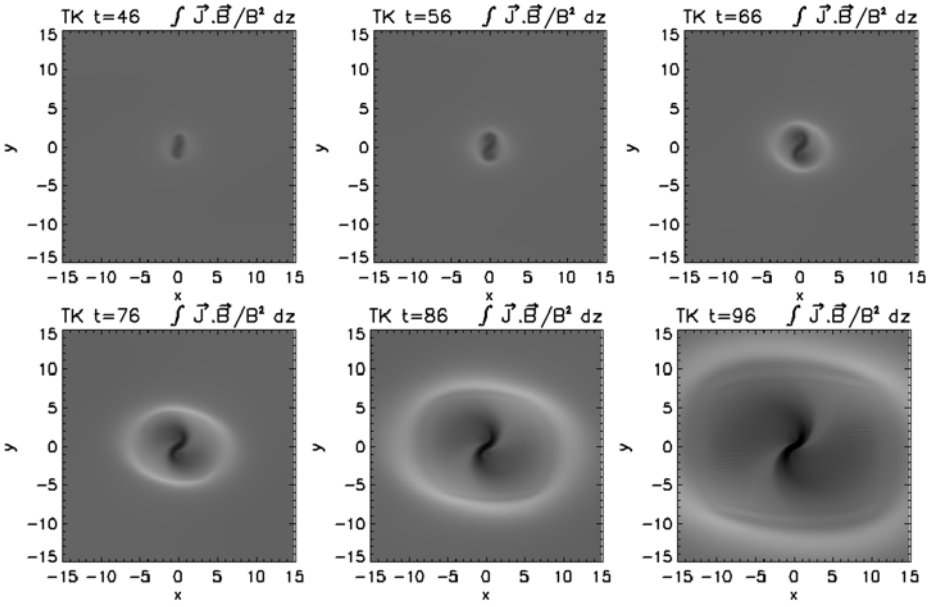

Figure 7 Same as Figure 6 for TK. The ellipse formed by the positive values of $\int \mathbf{J} \cdot \mathbf{B}/B^2 \, \mathrm{d}z$ has a similar behavior as in ADG.

4.2. Fast Expanding Ellipse

Although the S-shaped direct currents ($\int \mathbf{J} \cdot \mathbf{B}/B^2 \, \mathrm{d}z < 0$, shown in black) produce very intense typical sigmoids at the early stages of evolution of the system, the current shell ($\int \mathbf{J} \cdot \mathbf{B}/B^2 \, \mathrm{d}z > 0$, shown in white) may also produce coronal emission, which will appear only and suddenly after $t = 56$. To obtain a more quantitative analysis, we fit the shape of the current shell, integrated along the altitude, by an ellipse. The minor and major axes of the fitted ellipse increase in length and rotate during the expansion (plotted in the first three panels of Figures 8 and 9). It is noteworthy that the increasing horizontal expansion speed of the bright ellipse is nearly equal to the horizontal velocities of the plasma at the same locations in (x, y) at the altitudes z where the current shell is almost vertical (*i.e.*, where the contribution of $\mathbf{J} \cdot \mathbf{B}/B^2$ is maximal to the integral $\int \mathbf{J} \cdot \mathbf{B}/B^2 \, \mathrm{d}z$). The mean horizontal expansion velocity of the plasma in the current shell at locations where $\int \mathbf{J} \cdot \mathbf{B}/B^2 \, \mathrm{d}z > 0$ takes values in the range $\pm 10\%$ of its maxima; it is about $0.37\, c_\mathrm{A}$ at $t = 86$ and $0.55\, c_\mathrm{A}$ at $t = 96$ in ADG. The velocities are $0.43\ c_\mathrm{A}$ and $0.59\, c_\mathrm{A}$ at the same times in TK, respectively. Between $t = 86$ and $t = 96$, the velocities show a slight tendency towards saturation in both simulations.

Within the ellipse, the positive values of $\int \mathbf{J} \cdot \mathbf{B}/B^2 \, \mathrm{d}z$ at a given time vary from a minimum to a maximum value. Both extrema increase with time (see last panel in Figures 8 and 9), although in TK they eventually slowly decrease after $t = 86$. Figures 6 and 7 show that the maximal values of $\int \mathbf{J} \cdot \mathbf{B}/B^2 \, \mathrm{d}z > 0$ are located alongside the twisted flux tube. Naturally, they are associated with the asymmetric lobes in which the current layers are the narrowest (see Section 3.2).

It is also noteworthy that, although the positions of the minimal values of $\int \mathbf{J} \cdot \mathbf{B}/B^2 \, \mathrm{d}z > 0$ correspond well to the intersections of the major axis with the ellipse itself, the

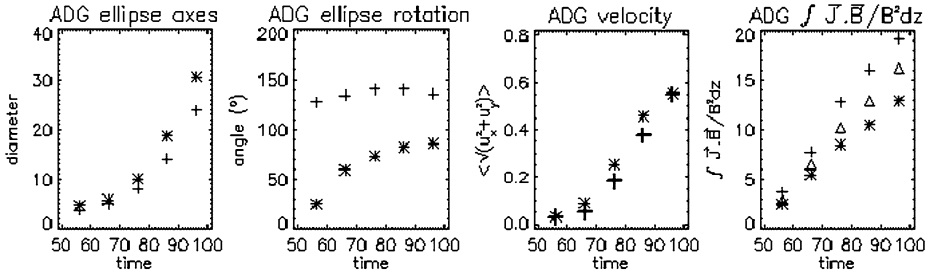

Figure 8 Temporal evolution of the current shell integrated along the z axis for ADG. From left to right are the lengths of the major (minor) axes of the ellipses that fit the shape of the positive values of $\int \mathbf{J} \cdot \mathbf{B}/B^2 \, \mathrm{d}z$, shown as stars (pluses), respectively; angles between the axis of the bipole (the y axis) and the line connecting the two maximum (minimum) values of $\int \mathbf{J} \cdot \mathbf{B}/B^2 \, \mathrm{d}z$ along the ellipse, shown as pluses (stars), respectively; mean horizontal velocity of the plasma in the current shell at locations where $\int \mathbf{J} \cdot \mathbf{B}/B^2 \, \mathrm{d}z > 0$ takes values in the range $\pm 10\%$ of its maxima (minima), shown as stars (pluses), respectively; and minimum values (shown as pluses), mean values (shown as triangles), and maximum values (shown as stars) of $\int \mathbf{J} \cdot \mathbf{B}/B^2 \, \mathrm{d}z$ within the ellipse.

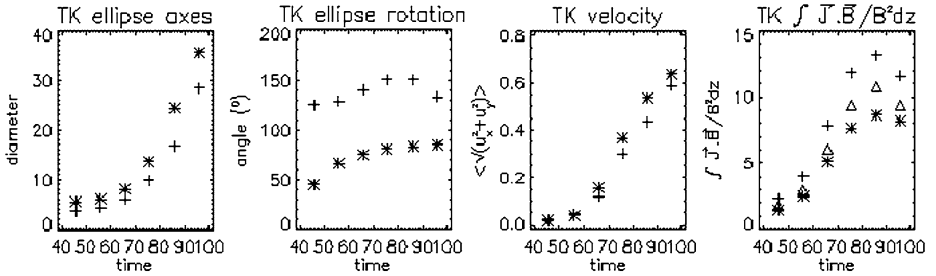

Figure 9 Same as Figure 8 for TK. The behavior of the ellipse is similar to that of ADG. Note that, because the simulation domain is much larger in TK than in ADG, $\int \mathbf{J} \cdot \mathbf{B}/B^2 \, \mathrm{d}z$ decreases after $t = 86$ (see discussion in Section 4.2. for details).

positions of the maximum values of $\int \mathbf{J} \cdot \mathbf{B}/B^2 \, \mathrm{d}z$ do not correspond to the intersections of the minor axis with the ellipse. The latter is a direct result from the integration along z. The integration over the whole z axis implies that the current density near the magnetic polarities is added to the current density at higher altitude. The current density close to the magnetic polarities is much more intense than the one higher, so the maximum of the integral is rooted near the magnetic polarities and does not rotate with the axes of the ellipse, which is caused by the rotation of the twisted magnetic flux tube. If we take into account that the EIT and SXR waves are coronal structures (*i.e.*, they evolve at quite high altitude), the dissipation of the current densities at low altitude would not be responsible for the observed structure. As no observation led to the estimation of the altitude of the structures, we continue to analyze the integration of $\int \mathbf{J} \cdot \mathbf{B}/B^2 \, \mathrm{d}z$ for all z inside the box of computation.

The minima of $\int \mathbf{J} \cdot \mathbf{B}/B^2 \, \mathrm{d}z > 0$ are located in two arcs that can be connected by a line that is nearly parallel to the axis of the twisted flux tube. Because the latter eventually becomes parallel to the x axis, as the flux tube rotates during its expansion, the angle between the line connecting the two minima of $\int \mathbf{J} \cdot \mathbf{B}/B^2 \, \mathrm{d}z > 0$ and the y axis (which is parallel to the orientation of the magnetic bipole) evolves in time from a few degrees to 90°. The corresponding rotation is quite fast at the beginning of the expansion of the flux tube, then it slows

down when the angle approaches 90°. The angular speed of the minima of $\int \mathbf{J}\cdot\mathbf{B}/B^2\,\mathrm{d}z > 0$ is about $1.4°/t_\mathrm{A}$ between $t = 76$ and $t = 96$, in the counterclockwise direction. The same angle for maximum values of $\int \mathbf{J}\cdot\mathbf{B}/B^2\,\mathrm{d}z$ ranges from 122° to 155°. For $t < 76$ the rotation is counterclockwise at an angular speed of $\approx 2.5°/t_\mathrm{A}$ in both codes and becomes clockwise for $76 < t < 96$ at an angular speed of $\approx 1°/t_\mathrm{A}$ in ADG and $\approx 2°/t_\mathrm{A}$ in TK. The current values that contribute the most to $\int \mathbf{J}\cdot\mathbf{B}/B^2\,\mathrm{d}z > 0$ are located inside the two lobes of the current shell at rather low altitude. The rotation of the lobes with respect to the axis of the twisted flux tube is obvious but the location of the maxima of $\int \mathbf{J}\cdot\mathbf{B}/B^2\,\mathrm{d}z > 0$ does not reproduce this rotation. The location of the maximum of $\mathbf{J}\cdot\mathbf{B}/B^2 > 0$, which is located inside the lobes, increases in altitude in the interval $46 < t < 76$ and follows the rotation of the lobes. For $t > 76$, its altitude decreases and returns to the magnetic polarities at $z = z°$ in which the current lobe is rooted. We argue that this inversion of rotation of the maximum of the $\mathbf{J}\cdot\mathbf{B}/B^2 > 0$ direction for $t > 76$ is a numerical artefact. Indeed, the current shell expands in every direction, towards regions that are treated by coarser grid points. There, the viscous effects become relatively important and lead to a broadening of the current layers, which results in lower electric current densities. This conjecture is supported by the behavior of the current shell in TK: for $t \geq 86$, it progressively takes a rectangular shape (see Figure 7). This is a reminiscent of the Cartesian mesh, which in these regions is more stretched than in ADG. We expect that the inversion of the rotation of $\int \mathbf{J}\cdot\mathbf{B}/B^2\,\mathrm{d}z > 0$ would not exist if the numerical grid of the simulations would have been constant. We also believe that this spatial resolution issue is also responsible for the aforementioned decrease of $\int \mathbf{J}\cdot\mathbf{B}/B^2\,\mathrm{d}z > 0$ for $t \geq 86$ with TK and for the overall larger $\mathbf{J}\cdot\mathbf{B}/B^2$ values in the shell for ADG as compared with TK (see Section 3.2).

5. Comparison with Two Observed EIT Waves

5.1. Applicability of the Model to Observations

The studied simulations incorporate the fast expansion of a twisted flux tube, originating from an isolated magnetic bipole. Even if there is neither loss of equilibrium nor instability of the twisted flux tube (as believed to happen in a CME), the expansion of the twisted magnetic flux tube shows properties similar to observed CMEs dynamics. First, the simulated twisted flux tube is accelerated towards a nearly constant speed (see also Török and Kliem, 2003), as observed in most CMEs (Zhang *et al.*, 2001). Second, filaments are often modeled as weakly twisted flux tubes (*e.g.,* Aulanier and Schmieder, 2002) and the axis of the modeled flux tube rotates as it expands; Webb *et al.* (2000) showed that during the halo CME produced on 12 May 1997 the eruptive filament rotated before it disappeared. Third, the S-shaped electric currents that are created under the twisted flux tube already before its dynamic expansion can be related to soft X-ray sigmoids, which are often observed before CMEs (Canfield, Hudson, and McKenzie, 1999).

So, assuming that the large-scale dipolar solar magnetic field only weakly influences the magnetic processes involved in the development of CME events that originate from isolated active regions, we compare the results of our model with two observed CMEs and their related EIT waves that took place in such configurations, namely the 7 April and 12 May 1997 events. The locations of the active regions at the time of the eruptions were not far from the central meridian of the Sun, leading to reduced projection effects. For both events, the related EIT waves were almost circular: they are among the (only) four circular EIT waves reported in the literature (see Section 1). The two remaining nearly circular EIT

waves both occurred on 24 September 1997 and were associated with an active region that was close to the solar limb. We do not compare our model with these two events because of large projection effects. Since the simulations give similar results, we used only the results of ADG (owing to its better spatial resolution) for comparison with the observations.

5.2. Spatial Dimensionalizing of the Model

The typical features that appear on the solar disk in CME events are sigmoids (before the CME) and coronal dimmings (during the CME). We use the Soft X-ray Telescope (SXT, Tsuneta *et al.*, 1991) onboard the *Yohkoh* satellite to analyze the sigmoids related to both studied events. The coronal dimmings can be observed in the 195 Å filter of the Extreme ultraviolet Imaging Telescope (EIT, Delaboudinière *et al.*, 1995) onboard the *Solar and Heliospheric Observatory* (SOHO). We also use line-of-sight magnetograms obtained with the Michelson and Doppler Imager (MDI/SOHO; Scherrer *et al.*, 1995) and with the Kitt Peak Vacuum Tower Telescope (VTT).

To reach the best match among all the observations, we first derotate them to the times of the eruptions as observed with EIT. Second, we subtract the EIT images of the EIT waves with a pre-event image to obtain the so-called Derotated Base Differenced Images (DBDIs; see Delannée, Hochedez, and Aulanier (2007) for details). The DBDIs are the only images that can show properly what is moving as the brightness increase or decrease inside the moving structures from one image to the following one do not interfere. This is not the case when producing running difference images.

We overlay the vertical component of the modeled magnetic field at the lower line-tied boundary of the numerical box onto the strongest magnetic polarities in the observed photospheric magnetograms available near the time of the eruptions (at 16:14:22 UT on 7 April 1997 obtained by the VTT and at 03:16:05 UT on 12 May 1997 obtained by MDI). These overlays are plotted in the upper panels of Figure 10, with contours showing the modeled $B_z = \pm 0.3$. Since the maximum in the model is $B_z = 1$ and the maximum of the observed line-of-sight magnetic fields is $b = 700$ G (1200 G) on 7 April (12 May), respectively, the $B_z = \pm 0.3$ contours should correspond to the observed photospheric values of $b_{\text{contours}} = 210$ G (360 G) on 7 April (12 May), respectively. We verified that both simulated and corresponding observed contours of the magnetic field are roughly overlying to produce the presented figures. This first overlay fixed the spatial correspondence between the simulation and the observations that we used to produce the following images.

In both active regions, a sigmoid was observed prior to the eruption. Sigmoids can be related to electric current sheets or extended electric current layers formed below expanding twisted flux tubes (Titov and Démoulin, 1999; Kliem, Titov, and Török, 2004; Aulanier, Démoulin, and Grappin, 2005; Aulanier, Pariat, and Démoulin, 2005). The sense of the sigmoids shape (forward or inverse "S") is a tracer of the dominant sign of magnetic helicity within an active region (Pevtsov, Canfield, and McClymont, 1997; Green *et al.*, 2007). The sigmoid on 7 April 1997 is S-shaped (indicating positive helicity) whereas the one on 12 May 1997 is inverse S-shaped (indicating negative helicity). Since the magnetic helicity is negative in our model, we mirrored the simulation results before overlaying them to the observations of the 7 April 1997 event. The panels in the second row of Figure 10 show the overlay between the contours of the direct currents from $\int \mathbf{J} \cdot \mathbf{B}/B^2 \, \mathrm{d}z$ prior to the dynamic phase (at $t = 56$) and the soft X-ray observations prior to the two EIT waves (at 13:32:58 UT on 7 April and at 04:32:02 UT on 12 May). The overlays are far

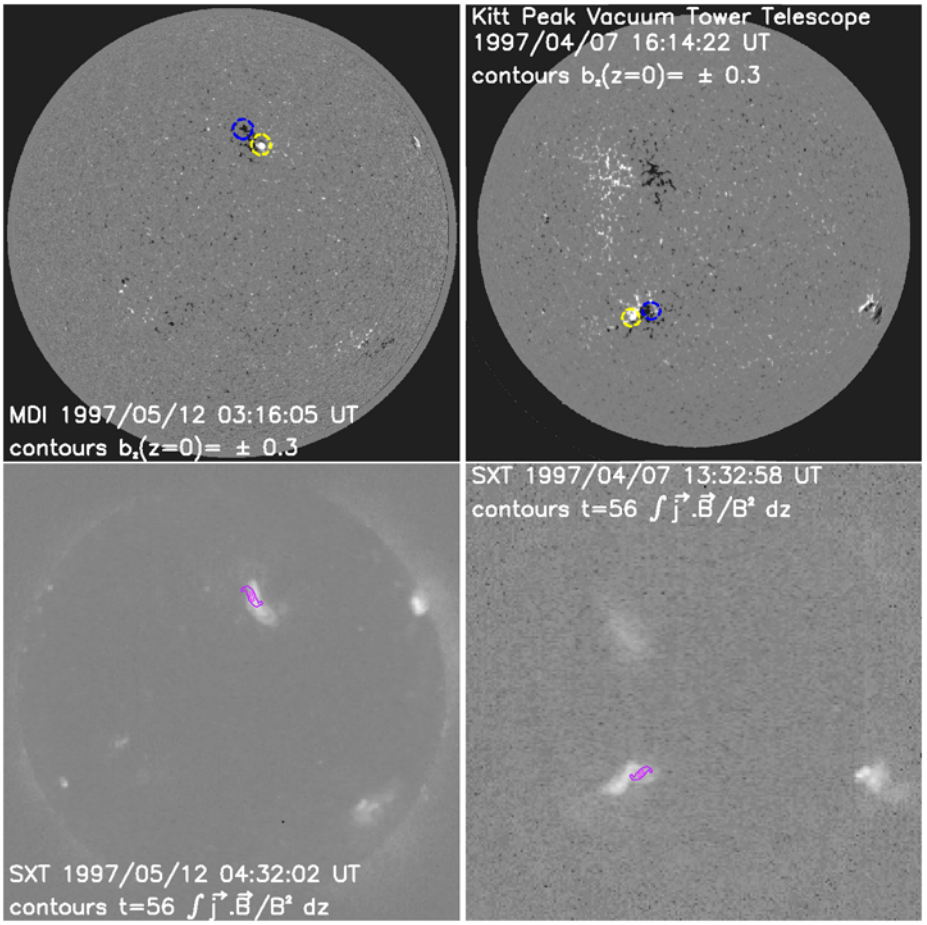

Figure 10 Overlay of observations of the active regions where the propagating EIT waves on 12 May 1997 (left column), and 7 April 1997 (right column), took place with quantities resulting from the ADG simulation. Top: MDI magnetogram, together with contours of B_z at $t = 6$. The blue contours show $B_z(x, y, 0) = -0.3$; the yellow contours show $B_z(x, y, 0) = +0.3$. Bottom: SXT observation obtained prior to the flare and contours of $\int \mathbf{J} \cdot \mathbf{B}/B^2 \, \mathrm{d}z = [-5.5; -4]$ at $t = 56$.

from being perfect: the alignments of the sigmoids with respect to the photospheric flux concentration, their lengths, and their asymmetries are poorly modeled. This discrepancy is due to the model prescriptions. The angle between the S-shaped current layer axis and the magnetic inversion line decreases with time (*i.e.*, with the twist). It is not possible to twist the system enough to obtain the observed alignment without getting its eruption first. Moreover, a symmetric magnetic configuration was modeled, whereas the observed active regions clearly show a leading polarity that is more compact than the trailing one. This last issue explains why the endpoints of the simulated sigmoids cannot extend as much into one of the magnetic polarities in the model as in the observed ones. Finally, even if the projection effects from the localization on the solar surface can be neglected at first, they still must play a role in spreading the observed sigmoids towards the nearest solar pole.

5.3. Temporal Dimensionalizing of the Model

To overlay the simulated $\int \mathbf{J}\cdot\mathbf{B}/B^2\,\mathrm{d}z$ at different times of the simulation with the observed propagating EIT wave, the model has to be dimensionalized in time. By definition, one time unit dt in the simulation is equal to a half Alfvén time (see Section 2.2). To estimate the coronal Alfvén time at coronal heights that correspond to the height z at which the current shell is the most vertical (*i.e.*, at which its contribution to $\int \mathbf{J}\cdot\mathbf{B}/B^2\,\mathrm{d}z$ is maximal), we construct an idealized magnetic model for both erupting active regions. We model each of the two bipolar active regions by a subphotospheric dipole of magnetic moment M, placed at a depth d. We choose the depth of the dipole equal to the distance L between the photospheric magnetic polarities ($d = L$). The following equations allows one to estimate the Alfvén time t_A:

$$t_\mathrm{A} = L/c_\mathrm{A}, \tag{14}$$

$$c_\mathrm{A} = b(\mu n m_\mathrm{p})^{-\frac{1}{2}}, \tag{15}$$

$$b = M\left[L\left(1+\frac{z}{2}\right)\right]^{-3}, \tag{16}$$

$$M = b_\circ L^3, \tag{17}$$

where $b_\circ$ is the maximum observed photospheric magnetic field inside the polarities, b is the magnetic field intensity in the corona at the modeled dimensionless altitude z, c_A is the Alfvén velocity, n is the density of particles per unit volume at the altitude z, and m_p is the proton mass. These settings lead to

$$t_\mathrm{A} = L b_\circ^{-1}(\mu n m_\mathrm{p})^{\frac{1}{2}}\left(1+\frac{z}{2}\right)^3. \tag{18}$$

The Alfvén time is therefore proportional to the distance between the observed polarities, to the square root of the coronal density inside the CME, and to the cube of the altitude at which the current shell contributes most to $\int \mathbf{J}\cdot\mathbf{B}/B^2\,\mathrm{d}z$, and it is inversely proportional to the observed maximum magnetic field of the magnetic polarities.

The altitude at which the current shell contributes most to $\int \mathbf{J}\cdot\mathbf{B}/B^2\,\mathrm{d}z$ is $9 < z < 13$ at $t = 86$. We note that taking this interval of z implicitly leads to the assumption that EIT waves are mainly coronal structures, which is expected since they are observed in coronal spectral emission lines. However, estimating the correspondence between the Alfvén time inside the box of computation ($t_\mathrm{A} = 2$ everywhere) and in the observation implies that the Alfvén time has the same value inside the erupting active region and far from it. This seems quite unreasonable from observational facts.

The maximum values of the observed magnetic field inside the erupting active regions related to the two studied EIT waves are $b_\circ = 700$ G (1200 G) on 7 April (12 May), respectively. In taking these values it is assumed that the observed bipoles have polarities with the same maximal intensities or at least the same magnetic fluxes. As already noted the polarities of the observed bipoles are different, with the maximum magnetic field in the leading polarities being much stronger (see the values just given) than in the trailing ones ($+325$ G on 7 April and -317 G on 12 May). As the trailing polarities are much wider than the leading ones, the magnetic fluxes of the two polarities are well balanced. This balance between the fluxes of the two magnetic polarities of each bipole reinforces the fact that they are merely linked to other magnetic polarities of the Sun.

Table 1 Parameters used to estimate the observational Alfvén times.

Date	$\Delta t_{\rm obs}$ (min)	L (Mm)	$b_\circ$ (G)	z	n (cm^{-3})	$t_{\rm A}$ (min)	Δt (min)
7 April 1997	9	51	700	11	4×10^8	3.82	19
					$1.\times10^8$	1.91	9.5
					0.72×10^8	1.29	9
				13	0.3×10^8	1.29	9
				9	1.9×10^8	1.29	9
12 May 1997	17	74	1200	11	4×10^8	3.23	25.84
					$1.\times10^8$	1.61	12.88
					1.73×10^8	2.13	17
				13	1.15×10^8	2.13	17
				9	7.4×10^8	2.13	17

As the value of the density n in a CME greatly varies in space and time, we computed the values of $t_{\rm A}$ for different n values. The altitudes in the current shell where the density current contributes the most to $\int \mathbf{J}\cdot\mathbf{B}/B^2\,{\rm d}z$ is $z \approx 11$, corresponding to $zL/2 \approx 280$ Mm (407 Mm) if we take the parameters for the EIT wave produced on 7 April 1997 (12 May 1997), respectively. The two altitudes are very close. These altitudes are coherent with that of the coronal wave front observed at the limb in the Large Angle Solar Coronograph (LASCO) C1 field of view by Schmieder *et al.* (2000). A coronal density of $n = 4\times10^8$ cm^{-3} was obtained by Akmal *et al.* (2001) in a CME, at an altitude of 343 Mm. Another density estimation of $n = 1\times10^8$ cm^{-3} was obtained inside a quiescent coronal loop at 343 Mm by Fort, Picat, and Dantel (1973). This value can be taken as a lower limit for the coronal density in the current shell, since in our model the latter is co-spatial with an enhanced density with respect to the surrounding corona. There exists a nearby n value for both events that results in an Alfvén time that allows a direct overlay (presented in Figure 11) of $\int \mathbf{J}\cdot\mathbf{B}/B^2\,{\rm d}z$ maps separated by $\Delta t = 14 = 7t_{\rm A}$ ($\Delta t = 16 = 8t_{\rm A}$) with the EIT wave observed on 7 April (12 May) in the DBDIs at time intervals $\Delta t_{\rm obs} = 9$ min ($\Delta t_{\rm obs} = 17$ min), respectively. At $z = [9; 13]$, the coronal densities implying the same Alfvèn times as just described are close (by a factor of three) to the values given by Akmal *et al.* (2001). Table 1 summarizes the parameters we use to estimate the Alfvén times for the two observed events.

5.4. EIT Waves and Current Shells Overlay

Using the spatial and temporal scaling just described, we now compare the structure and dynamics of the positive values of $\int \mathbf{J}\cdot\mathbf{B}/B^2\,{\rm d}z$ with the evolution of the EIT waves that we highlight in the DBDIs. The contours of the current shell and the EIT waves are both almost circular. Both EIT waves incorporate two bright patches located at opposite sides of the corresponding active regions and faint patches located between the bright patches. The maximum and minimum of the observed intensity in the EIT waves and of the positive values of $\int \mathbf{J}\cdot\mathbf{B}/B^2\,{\rm d}z$ match spatially. Both are expanding and slightly rotating.

We find that the velocities of $\int \mathbf{J}\cdot\mathbf{B}/B^2\,{\rm d}z$ correspond to 363 km s^{-1} with the observed parameters of 7 April 1997 and to 249 km s^{-1} with the observed parameters of 12 May

1997. Klassen *et al.* (2000) report 369 km s^{-1} for the April 7 EIT wave. Thompson *et al.* (1998) report 255 km s^{-1} for the 12 May EIT wave. The simulated and observed values of the velocity are hence in very good agreement for both EIT waves.

If we discard the late clockwise motions for the maximal values of $\int \mathbf{J} \cdot \mathbf{B}/B^2 \, dz > 0$ (as discussed in Section 4.2), the modeled EIT wave rotates counterclockwise at about 0.47° min^{-1} on 12 May 1997. The rotation of the brightest patches of this EIT wave, detected by Podladchikova and Berghmans (2005), is of the order of $0.36 - 0.60^\circ$ min^{-1} counterclockwise. So the modeled and observed rotations are of the same order.

5.5. Discussion

Warmuth *et al.* (2004) showed that many EIT waves other than those presented in this study are decelerating during their propagation from their active region source. Our model shows that, on the contrary, the expanding velocity is constantly increasing. We note that in the model the upward velocity of the current shell saturates at late times, so we may expect that its horizontal velocity may do the same after a certain expansion. We also believe that the spherical geometry and large-scale complex magnetic topologies can play a significant role in the decelerating (and maybe halting) process of the EIT wave (see Delannée, Hochedez, and Aulanier, 2007).

Moreton waves are part of the same structure that produces EIT waves (Warmuth *et al.*, 2004; Delannée, Hochedez, and Aulanier, 2007). So, if expanding current shells can model EIT waves, they should also reproduce the Moreton waves. We argue here from modeling facts for the same idea developed by Balasubramaniam, Pevtsov, and Neidig (2007) and Warmuth (2007) from observational facts: Moreton waves are coronal structures. Since Moreton waves are observed in Hα, they should a priori be chromospheric low-lying structures, which cannot correspond to Joule heating at low altitudes in current shells such as those modeled in this paper; indeed, the latter almost do not move at low altitudes (see Figures 2 and 3). If propagating Moreton waves still occur within current shells, they must therefore occur at high coronal altitudes. This could be possible only if cool Hα emitting material could there be formed within the hot coronal material visible in EUV. This is not straightforward. However, we have shown that enhanced densities are generated within the current shells, with a density contrast of a factor of two, so thermal instabilities may occur there (*e.g.,* Oran, Mariska, and Boris, 1982). If such instabilities take place, they naturally result in cooling and condensing of the plasma, after it has been compressed in the shell and further heated by Joule dissipation. This process is often used to interpret the formation of prominence condensations (Karpen, Antiochos, and Klimchuk, 2006) and of postflare loops (Schmieder *et al.*, 1995). In these cases the instability rates are far too long to explain the formation of Moreton waves within EIT waves if the typical temperature of the structure is higher than 10^7 K but the cooling time could be very short if the typical temperature of the structure is lower than 10^6 K. This interesting issue will have to be addressed in the future.

By construction, our model cannot produce a flare since no vertical current sheet forms in the trailing part of the flux tube during its expansion. So we cannot discuss the time relation between the observed flares and the related EIT waves. However, we note that the location of appearance of the EIT wave front is not close to the magnetic dipole, but rather far from it. The ellipse first appears with a major axis of already about five nondimensional length units in the simulation (see first panel in Figure 8), which corresponds to 185 Mm on 12 May 1997 and 127 Mm on 7 April 1997. These distances are in good agreement with the 100 Mm value between the first appearance of Moreton waves and the flare site found by Warmuth (2007). Our model gives a simple answer to the impossibility of observing wave

fronts closer to the flare site: the EIT waves are independent of the occurrence and location of a flare; they only depend on the dynamics of CME-related expanding flux tubes.

6. Relation between EIT Waves and Halo CMEs

The two CMEs that are associated with the EIT waves on 7 April and 12 May 1997 were observed using the LASCO C2 instrument on SOHO. As we did with the EIT images, we also subtract the images of the CMEs with a pre-event image to highlight the CME feature above the occulting disk, thus producing Based Difference Images (BDIs).

6.1. Shape and Brightness

In our model, the EIT waves are a direct counterpart of CMEs. Therefore, we should find a way to compare observationally the appearance of the EIT waves and their related halo CMEs. As the EIT waves are produced in the outer layer of an expanding flux rope, they should also be spatially very closely related to the dimmings produced by the plasma depletion on the solar disk during the CME. This fact is actually observed by Podladchikova and Berghmans (2005). Both CMEs clearly show two bright patches. On 12 May 1997 the brightest patches are located in the equatorial streamers whereas on 7 April 1997 they are located in the southeast and northwest quadrants of the corona. These halos also show fainter patches, located in the northern hemisphere on 12 May 1997 and in the northeast and southwest quadrants on 7 April 1997. It is worth noting that the observed locations of the brighter and fainter patches of the EIT waves and their halo CMEs have the same shape and appear in the same quadrants. The approximate alignment of these brighter and fainter patches of both the CME and the related EIT wave can be possible despite the early rotation of the brightest patches of the EIT wave because, as explained in the Section 4.2, the rotation of the patches approach a limit that is reached when the twisted flux tube is approximately aligned with the magnetic neutral line in the active region. This limit should have been reached when the CME became visible in the LASCO C2 field of view, two hours after the EIT wave has disappeared in the EIT field of view.

We have shown in Section 3.3 that the current shell is fully co-spatial with an enhanced-density shell. Therefore, we can further compare the morphology of the current shell with the observed CMEs, even if LASCO C2 observations are only sensitive to density and not to temperature variations. We mention here that if the LASCO C2 observations are sensitive to only density, spectroscopic data revealed that the plasma in the CME is heated during its propagation (Akmal *et al.*, 2001). The current shell present in this simulation could be the cause of the heating process during the plasma ejection. Figure 12 shows overlays of the EIT DBDIs of the EIT wave, of the LASCO C2 BDIs of the related halo CMEs, and of the same transparent isosurfaces of the current shell as plotted in Figures 2 and 3. The latter are tilted to match the heliospheric coordinates of the erupting active regions and the shapes of the sigmoids and the active regions. This projection assumes that the flux tube vertical expansion is aligned with the solar radius.

Our model is described in Cartesian coordinates, which do not take into account the spherical symmetry of the Sun. Since the magnetic field lines are extending approximately radially from the solar surface into the corona, the lateral expansion of the current shell in a spherical coordinate system model should be slightly larger than what is presented in Figure 12, but not very different. Figure 12 suggests that, if the twisted flux tube has slightly rotated further than what is shown at the plotted times (*i.e.*, when it would appear in the

LASCO C2 field of view), the brightest patches of the halos may exactly correspond to the locations of the lobes where the maxima of $\mathbf{J} \cdot \mathbf{B}/B^2$ are located within the shell. The fainter locations of the halos would then naturally correspond to the minima of $\mathbf{J} \cdot \mathbf{B}/B^2$ within the shell.

Since on 12 May 1997 the erupting active region is in the northern hemisphere (with coordinates of N21W06.5 as given by Thompson *et al.* (1998)), the nearly radially expanding current shell naturally appears first in the northern hemisphere of the corona. This nicely fits the observed halo CME. On 7 April 1997 the active region is located at E11S21, so the current shell is not viewed from above, but rather in projection, which makes it look asymmetric; the eastern lobe of the current shell is visible in almost its full vertical length. The fact that the halo CME first appears in the southeast quadrant of the LASCO C2 field of view is also consistent with the current shell orientation. This leading edge corresponds almost to the top of the shell. It is remarkable that the isosurface of $\mathbf{J} \cdot \mathbf{B}/B^2 = 1.9$ (drawn in red in the lower panel in Figure 12) has a shape very similar to the sootheastern part of the leading edge of the halo CME. Similarly, the other lobe of the current shell, located westwards of the erupting active region, and appearing there as a sheetlike feature, corresponds well with the shapes of the western parts of both the EIT wave and the halo CME.

6.2. Association between CME and EIT Wave Velocities

Our model therefore readily interprets halo CMEs as the continuity of the EIT wave: the halo CME becomes visible when the associated current and enhanced-density shell, projected onto the plane of the sky, expands beyond the occulting disk of the coronagraph. In our simulation, at the time corresponding to the observations of the EIT waves at 05:07:10 UT on 12 May 1997 and 14:12:38 UT on 7 April 1997, the top of the current and enhanced-density shell in the simulation has reached a height of 2.6 solar radii (see Figures 11 and 12). This supports the idea that EIT waves are not low-altitude phenomena, but rather high-altitude 3D structures projected onto the solar disk.

Since the erupting active region on 12 May 1997 is close to the Sun's center, we can, in a first approximation, neglect projection effects and estimate the velocity of the leading edge of the halo CME. When the EIT wave is observed at 05:07:10 UT (corresponding to $t = 96$ in the simulation), the top of the current and enhanced-density shell has reached a height of 2.6 solar radii in the simulation. At this altitude, many CMEs have already reached a nearly constant velocity. In the simulation, we see a tendency of saturation towards a constant velocity of the current shell at $t \geq 86$ (Figure 1; see also Török and Kliem, 2003). In the LASCO C2 field of view, the halo CME expansion is also nearly constant and the velocity of the lateral expansion of the current and the enhanced-density shell should be nearly constant between $t = 96$, corresponding to the observation of the EIT wave at 05:07:10 UT, and $t = 178$, corresponding to the observation of the halo in LASCO C2 at 07:35 UT (see Figure 12). (The time difference between the LASCO C2 image and the EIT image is 88 min; by using the values given in Table 1, this corresponds to a time gap of $\Delta t = 41 t_{\mathrm{A}} = 82$ in the simulation.) In that case, the model predicts that the velocities of the EIT wave and its related CME produced in the configuration of 12 May 1997 are nearly the same, which was actually noticed by Thompson *et al.* (1998). Webb *et al.* (2000) argued that such a relation between the EIT wave and the related halo speeds is very rare, which seems to be true as it happens only if the eruption occurs near the disk center owing to the absence of projection effects.

On 7 April 1997 we estimate the southeastern leading edge CME velocity at 617 km s^{-1}, whereas Klassen *et al.* (2000) determined a velocity of 369 km s^{-1} of the EIT wave from

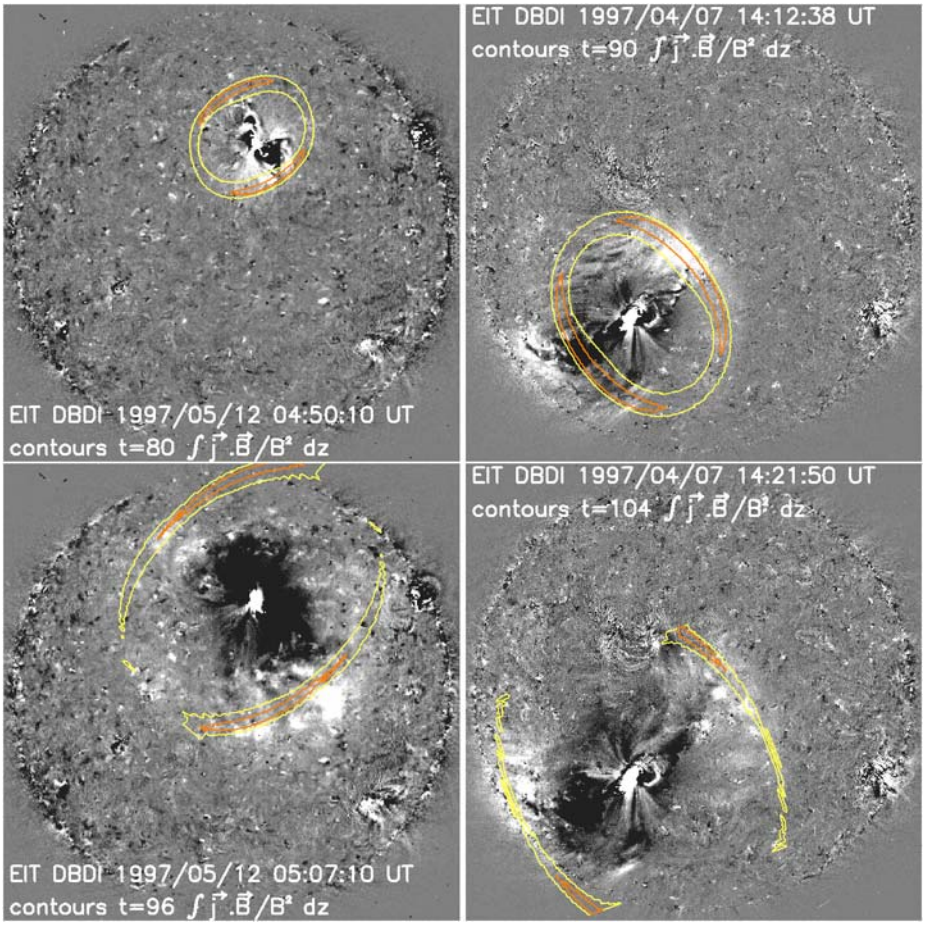

Figure 11 Overlay of observations of the propagating EIT waves on 12 May 1997 (left column), and 7 April 1997 (right column), with quantities resulting from the ADG simulation. Top: first EIT DBDIs of the EIT waves at 04:50:10 UT and 14:12:38 UT, respectively, together with contours of $\int \mathbf{J} \cdot \mathbf{B}/B^2 \, \mathrm{d}z = [8; 13]$ at $t = 80$ and $t = 90$, respectively. Bottom: second EIT DBDIs of the EIT waves at 05:07:10 UT and 14:21:50 UT, respectively, together with contours of $\int \mathbf{J} \cdot \mathbf{B}/B^2 \, \mathrm{d}z = [13; 18]$ at $t = 96$ and $t = 104$, respectively. The DBDIs are obtained from correcting the EIT images for the differential rotation of the Sun to the time of a pre-event image and subtracting the pre-event images afterwards. The times of the pre-event images are 04:16:48 UT on 12 May 1997 and 14:00:03 UT on 7 April 1997.

its two first positions visible on the opposite side from the active region center. The EIT wave bright front is visible moving towards the northwest. We estimate 379 $\mathrm{km\,s^{-1}}$ for the northwestern leading edge of the CME. So, the EIT wave front and the CME leading edge parts propagating towards the northwest have approximately the same velocities. The model given in this study can again reconstruct consistency among all these observational facts. On 7 April 1997 the expanding current and enhanced-density shell is tilted, so the southeastern leading edge almost corresponds to the top of the current and enhanced-density shell. In the simulations, the velocity of the top of this shell is about $1.2\,c_\mathrm{A}$ at $t = 96$ (see Figure 1), which is almost twice its lateral velocity ($0.55\,c_\mathrm{A}$, as given in Section 4.2). The observed southeastern velocity is approximately twice the northwestern velocity of the CME. We note that

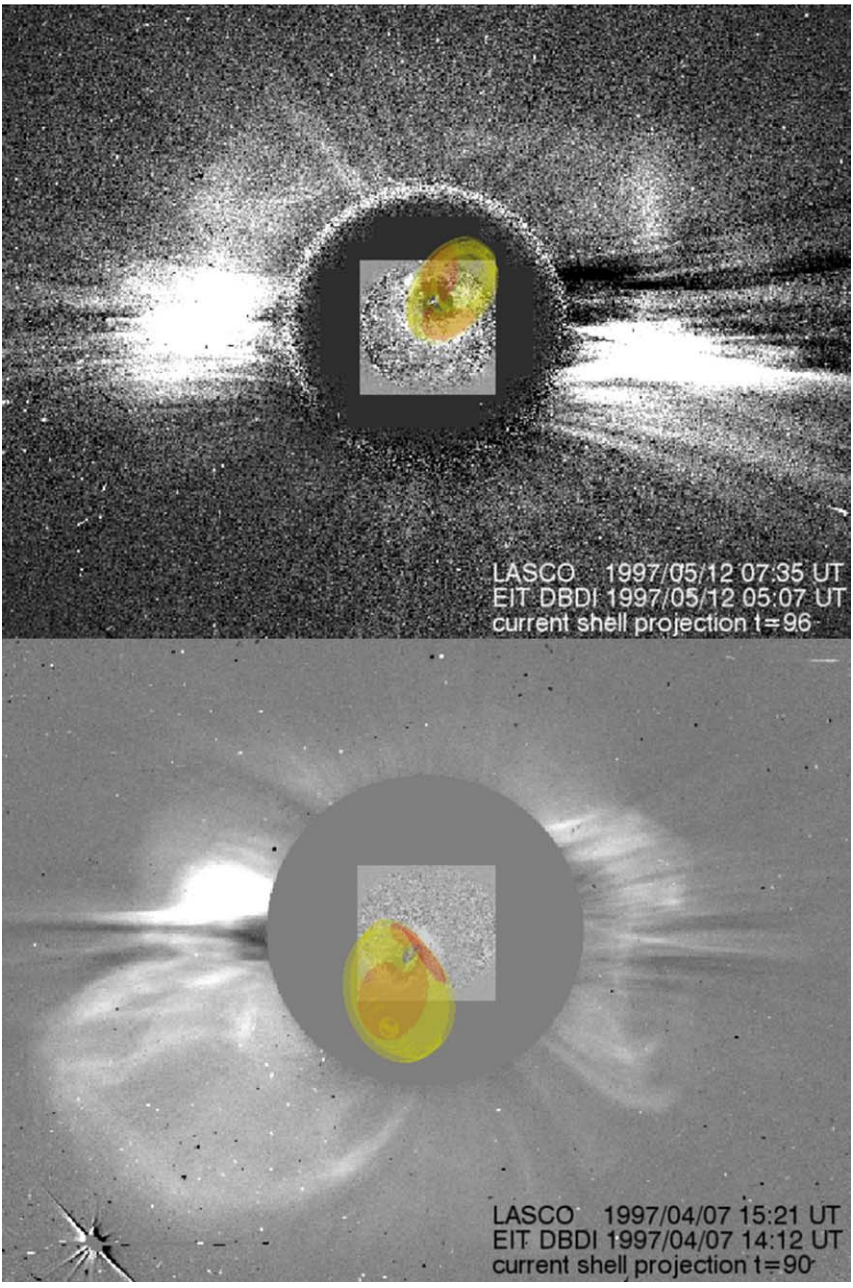

Figure 12 Overlay of observations of the propagating EIT waves and related CMEs on 12 May 1997 (top), and 7 April 1997 (bottom), with quantities resulting from the ADG simulation. The LASCO C2 images are obtained using the orange filter and after subtraction of pre-event images obtained at 05:28:54 UT on 12 May and at 14:26:29 UT on 7 April, respectively. The EIT DBDIs are identical to those presented in Figure 11. The current shell is rendered using the same procedure as in Figures 2 and 3. The tilt of the current shell matches the heliographic coordinates of the observed magnetic polarities, under the assumption that the expansion of the current shell is vertical to the solar surface.

the Web page http://cdaw.gsfc.nasa.gov/CME_list/UNIVERSAL/1997_04/jsmovies/1997_04/19970407.142744.p123g/c2_rdif.html provides a good view of the observations that can be understood in the light of the expanding current and enhanced-density shell model that we present here. One can see on the movie presented there that the brightest patches of the EIT wave and the halo CME are nicely following each other with similar speeds in each solar quadrant in which they are propagating.

7. Conclusion

Our study presents an alternative model for the propagating wavelike structures named EIT waves, Moreton waves, and SXI waves. In contrast to the usually used magnetosonic wave model, our model takes into account that EIT waves are always associated with CMEs, thus with eruptive flares, but never with confined flares. Our model is based on numerical simulations of the fast expansion of a 3D twisted flux tube in a single bipolar magnetic field region. Therefore this model can only be associated with active regions that are not magnetically linked to other active regions. Only very few EIT waves are observed in such a simple magnetic configuration. We could test our model only on two events (12 May 1997 and 7 April 1997).

The modeled flux tube is slowly twisted by photospheric vortex motions, centered at the two flux concentrations of a bipolar magnetic field. We find that return electric currents are generated at the outer edge of the expanding flux tube. These currents amplify and progressively evolve into a large-scale current shell surrounding the flux tube in the dynamic phase of its evolution. The weaker currents in the shell appear to occur mainly because of the compression between the expanding flux tube and its surrounding potential fields, whereas the stronger currents are associated additionally with the rotation of the flux tube axis during its expansion. A shell of enhanced density also occurs in the model, co-spatially with the current shell, but less contrasted with its surroundings. As the twisted magnetic flux tube expands in altitudes, it also inflates horizontally, pushing the two shells in altitude and horizontally.

The integration along the altitude of the current shell reveals a structure whose morphology and dynamics are very similar to observed EIT waves: both are almost circular, with two maxima and two minima of intensity, which are symmetric with respect to the center of the erupting active region. Both EIT waves and integrated current shell are rotating and expanding at a significant fraction of the Alfvén speed. From this we conjecture that EIT waves are due to Joule heating in current shells and/or due to plasma compression in enhanced-density shells, which are both created at the outer layer of an expanding twisted magnetic flux tube during a CME and observed from above, integrated along the line of sight.

The current and enhanced-density shell in our model can also be compared to the CMEs related to EIT waves. We note that the two observed halo CME and the EIT wave fronts that propagate in the same direction have similar shapes and velocities, indicating that the halo CME front is the continuation of the EIT wave.

According to our model, the legs of CMEs should extend to the moving bright front of EIT waves when the erupting active region is close to the solar limb. This interpretation differs from that of Vršnak *et al.* (2005), who observed in one case that an SXI wave is not located at the CME footpoints. However, Vršnak *et al.* (2005) just present a sketch but no images that would prove their interpretation. The STEREO/SECCHI instrument will be very well suited to address these issues as it will provide two observation angles of the same EIT wave event.

Our model is based on the assumption that the current shell can brighten the coronal plasma via Joule heating. The density increase is expected to have the same effect on the brightness of the coronal plasma observed in a large spectral band pass. Therefore, spectroscopic data are clearly needed to determine which of the two quantities is mainly responsible for the brightness of the moving front of the waves. *Hinode*/EIS could be used to test this.

The density model used in this paper was chosen so that the initial Alfvén velocity is unity in the whole simulation box. A parametric study of the response of the system to various density profiles will have to be done to investigate better the formation of the enhanced-density shell. We also need to estimate the influence of the velocities of the twisting motions on the formation and the behavior of the current shell. Titov and Démoulin (1999) produced a model of a twisted magnetic flux tube without any return current. Running a simulation of the expansion of this flux tube (as in Török and Kliem, 2005) would be needed to test for the possible formation or absence of a thin current shell in such a system. We expect that a current shell surrounding the expanding flux rope will generically form in any 3D flux rope eruption model. The 3D computation is essential for our result. Chen *et al.* (2002) simulated the vertical expansion of a magnetic flux tube in two dimensions to find the signature of EIT and Moreton waves. In two dimensions, a flux tube is in fact an isolated magnetic island that can neither inflate in all three spatial directions nor rotate. These motions, however, are essential to produce the shape and the contrast with the surroundings of the current and the enhanced-density shell we found in our simulations.

EIT waves produced in almost purely bipolar magnetic field configurations are very rare because of the general presence of several active regions on the solar surface that can magnetically interact. Delannée and Aulanier (1999) and Delannée, Hochedez, and Aulanier (2007) showed that in quadrupolar magnetic topologies, parts of EIT waves can remain stationary for about one hour. Chen, Fang, and Shibata (2005) simulated the rise of a twisted flux tube in a quadrupolar magnetic field in two dimensions and found the signature of a stationary wave at the footpoint of jumps of magnetic field line connectivity. A similar simulation, but in three dimensions, will have to be carried out to investigate the generation of both stationary and propagating structures of electric currents during the expansion of a twisted flux tube.

Acknowledgements SOHO is a project of international cooperation between ESA and NASA. T.T. is grateful for the support by the HPC-Europa programme, funded under the European Commission's Research Infrastructures activity of the Structuring the European Research Area programme, Contact No. RII3-CT-2003-506079, and for the warm hospitality of the solar group during his stay at LESIA. G.A. thanks UCL for travel support during his visit to MSSL. The numerical calculations were performed on the Compaq-HP Quadri-Opteron computers in Paris Observatory/SIO and on the IBM eServer p690 at CNRS/IDRIS. Financial support by the European Commission through the SOLAIRE Network (MTRN-CT-2006-035484) is gratefully acknowledged.

References

Akmal, A., Raymond, J.C., Vourlidas, A., Thompson, B., Ciaravella, A., Ko, Y.-K., Uzzo, M., Wu, R.: 2001, *Astrophys. J.* **553**, 922.
Aly, J.J.: 1989, *Solar Phys.* **19**, 120.
Amari, T., Luciani, J.F., Aly, J.J., Tagger, M.: 1996, *Astrophys. J.* **466**, L39.
Attrill, G., Harra, L., van Driel-Gesztelyi, L., Démoulin, P.: 2007, *Astrophys. J.* **656**, L101.
Aulanier, G., Schmieder, B.: 2002, *Astron. Astrophys.* **386**, 1106.
Aulanier, G., Démoulin, P., Grappin, R.: 2005, *Astron. Astrophys.* **430**, 1067.
Aulanier, G., Pariat, E., Démoulin, P.: 2005, *Astron. Astrophys.* **444**, 961.
Balasubramaniam, K.S., Pevtsov, A.A., Neidig, D.F.: 2007, *Astrophys. J.* **658**, 1372.
Biesecker, D.A., Myers, D.C., Thompson, B.J., Hammer, D.M., Vourlidas, A.: 2002, *Astrophys. J.* **569**, 1009.

Brown, D.S., Nightingale, R.W., Alexander, D., Schrijver, C.J., Metcalf, T.R., Shine, R.A., Title, A.M., Wolfson, C.J.: 2003, *Solar Phys.* **216**, 79.
Canfield, R.C., Hudson, H.S., McKenzie, D.E.: 1999, *Geophys. Res. Lett.* **26**, 627.
Chen, P.F.: 2006, *Astrophys. J.* **641**, L153.
Chen, P.F., Fang, C., Shibata, K.: 2005, *Astrophys. J.* **622**, 1202.
Chen, P.F., Wu, S.T., Shibata, K., Fang, C.: 2002, *Astrophys. J.* **572**, L99.
Cliver, E.W., Laurenza, M., Storini, M., Thompson, B.J.: 2005, *Astrophys. J.* **631**, 604.
Delaboudinière, J.-P., Artzner, G.E., Brunaud, J., Gabriel, A.H., Hochedez, J.-F., Millier, F., *et al.*: 1995, *Solar Phys.* **162**, 291.
Delannée, C.: 2000, *Astrophys. J.* **545**, 512.
Delannée, C., Aulanier, G.: 1999, *Solar Phys.* **190**, 107.
Delannée, C., Hochedez, J.-F., Aulanier, G.: 2007, *Astron. Astrophys.* **465**, 603.
Démoulin, P.: 2006, *Adv. Space Res.* **37**, 1269.
Fort, B., Picat, J.P., Dantel, M.: 1973, *Astron. Astrophys.* **24**, 267.
Green, L., Kliem, B., Török, T., van Driel-Gesztelyi, L., Attrill, G.: 2007 *Solar Phys.*, submitted.
Karpen, J.T., Antiochos, S.K., Klimchuk, J.A.: 2006, *Astrophys. J.* **637**, 531.
Klassen, A., Aurass, H., Mann, G., Thompson, B.J.: 2000, *Astrophys. J. Suppl.* **141**, 357.
Kliem, B., Titov, V.S., Török, T.: 2004, *Astron. Astrophys.* **413**, L23.
Low, B.C., Wolfson, R.: 1988, *Astrophys. J.* **324**, 574.
Magara, T., Longcope, D.: 2001, *Astrophys. J.* **559**, L55.
Manoharan, P.K., van Driel-Gesztelyi, L., Pick, M., Démoulin, P.: 1996, *Astrophys. J.* **468**, 73.
Mikic, Z., Schnack, D., van Hoven: 1990, *Astrophys. J.* **361**, 690.
Moreton, G.E.: 1960, *Astron. J.* **65**, 494.
Ofman, L., Thompson, B.J.: 2002, *Astrophys. J.* **574**, 440.
Oran, E.S., Mariska, J.T., Boris, J.P.: 1982, *Astrophys. J.* **254**, 349.
Pevtsov, A.A., Canfield, R.C., McClymont, A.N.: 1997, *Astrophys. J.* **481**, 973.
Podladchikova, O., Berghmans, D.: 2005, *Solar Phys.* **228**, 265.
Scherrer, P.H., Bogart, R.S., Bush, R.I., Hoeksema, J.T., Kosovichev, A.G., Schou, J., *et al.*: 1995, *Solar Phys.* **162**, 129.
Schmieder, B., Heinzel, P., Wiik, J.E., Lemen, J., Anwar, B., Kotrc, P., Hiei, E.: 1995, *Solar Phys.* **156**, 337.
Schmieder, B., Delannée, C., Deng, Y.Y., Vial, J.C., Madjarska, M.: 2000, *Astron. Astrophys* **358**, 728.
Shiota, D., Isobe, H., Chen, P.F., Yamamoto, T.T., Sakajiri, T., Sibata, K.: 2005, *Astron. Astrophys.* **634**, 663.
Titov, S., Démoulin, P.: 1999, *Astron. Astrophys.* **351**, 707.
Török, T., Kliem, B.: 2003, *Astron. Astrophys.* **406**, 1043.
Török, T., Kliem, B.: 2005, *Astrophys. J.* **630**, L97.
Thompson, B.J., Plunkett, S.P., Gurman, J.B., Newmark, J.S., St. Cyr, O.C., Michels, D.J.: 1998, *Geophys. Res. Lett.* **25**, 2461.
Thompson, B.J., Gurman, B.J., Neupert, Newmark, J.S., Delaboudinière, J.-P., St. Cyr, O.C., *et al.*: 1999, *Astrophys. J.* **517**, L151.
Thompson, B.J., Reynolds, B., Aurass, H., Gopalswamy, N., Gurman, J.B., Hudson, H.S., *et al.*: 2000a, *Solar Phys.* **193**, 161.
Thompson, B.J., Cliver, E.W., Nitta, N., Delannée, C., Delaboudinière, J.-P.: 2000b, *Geophys. Res. Lett.* **27**, 1431.
Tsuneta, S., Acton, L., Bruner, M., Lemen, J., Brown, W., Caravalho, R., *et al.*: 1991, *Solar Phys.* **136**, 37.
Uchida, Y.: 1968, *Solar Phys.* **4**, 30.
Vršnak, B.: 2001, *J. Geophys. Res.* **106**, 25249.
Vršnak, B., Warmuth, A., Temmer, M., Veronig, A., Magdalenič, J., Hillaris, A., Karlický, M.: 2005, *Astron. Astrophys.* **448**, 739.
Wang, Y.M.: 2000, *Astrophys. J.* **543**, L89.
Warmuth, A.: 2007, In: Klein, L., MacKinnon, A. (eds.) *The hight Energy Solar Corona: Waves, Eruptions, Particles*, *Lecture Notes in Physics* **725**, Springer, Berlin, 107.
Warmuth, A., Vršnak, B., Magdalenić, J., Hanslmeier, A., Otruba, W.: 2004, *Astron. Astrophys.* **418**, 1101.
Webb, D.F., Leping, P.R., Burlaga, L., DeForest, C., Larso, D., Martin, S., *et al.*: 2000, *J. Geophys. Res.* **105**, 27251.
Wills-Davey, M.J., Thompson, B.J.: 1999, *Solar Phys.* **190**, 467.
Wu, S.T., Zheng, H., Wang, S., Thompson, B.J., Plunkett, S.P., Zhao, X.P., Dryer, M.: 2001, *J. Geophys. Res.* **106**, 25089.
Wu, S.T., Li, B., Wang, S., Zheng, H.: 2005, *J. Geophys. Res.* **100**, A11102.
Zhang, J., Dere, K.P., Howard, R.A., Kundu, M.R., White, S.M.: 2001, *Astrophys. J.* **559**, 452.
Zhukov, A., Auchère, F.: 2004, *Astron. Astrophys.* **427**, 705.